Available online at www.sciencedirect.com

ScienceDirect

Geochimica et Cosmochimica Acta 178 (2016) 1–19

Geochimica et Cosmochimica Acta

www.elsevier.com/locate/gca

Olivine and melt inclusion chemical constraints on the source of intracontinental basalts from the eastern North China Craton: Discrimination of contributions from the subducted Pacific slab

Hong-Yan Li [a,*], Yi-Gang Xu [a], Jeffrey G. Ryan [b], Xiao-Long Huang [a], Zhong-Yuan Ren [a], Hua Guo [a], Zhen-Guo Ning [c]

[a] *State Key Laboratory of Isotope Geochemistry, Guangzhou Institute of Geochemistry, Chinese Academy of Sciences, Guangzhou 510640, China*
[b] *School of Geosciences, University of South Florida, Tampa, FL 33620, United States*
[c] *Shandong Institute of Geological Survey, Jinan 250013, China*

Received 25 October 2014; accepted in revised form 19 December 2015; available online 28 January 2016

Abstract

Contributions from fluid and melt inputs from the subducting Pacific slab to the chemical makeup of intraplate basalts erupted on the eastern Eurasian continent have long been suggested but have not thus far been geochemically constrained. To attempt to address this question, we have investigated Cenozoic basaltic rocks from the western Shandong and Bohai Bay Basin, eastern North China Craton (NCC), which preserve coherent relationships among the chemistries of their melt inclusions, their hosting olivines and their bulk rock compositions. Three groups of samples are distinguished: (1) high-Si and (2) moderate-Si basalts (tholeiites, alkali basalts and basanites) which were erupted at ~23–20 Ma, and (3) low-Si basalts (nephelinites) which were erupted at <9 Ma. The high-Si basalts have lower alkalies, CaO and FeO^T contents, lower trace element concentrations, lower La/Yb, Sm/Yb and Ce/Pb but higher Ba/Th ratios, and lower ε_{Nd} and ε_{Hf} values than the low-Si basalts. The olivines in the high-Si basalts have higher Ni and lower Mn and Ca at a given Fo value than those crystallizing from peridotite melts, and their corresponding melt inclusions have lower CaO contents than peridotite melts, suggesting a garnet pyroxenitic source. The magmatic olivines from low-Si basalts have lower Ni but higher Mn at a given Fo value than that of the high-Si basalts, suggesting more olivine in its source. The olivine-hosted melt inclusions of the low-Si basalts have major elemental signatures different from melts of normal peridotitic or garnet pyroxenitic mantle sources, pointing to their derivation from a carbonated mantle source consisting of peridotite and garnet pyroxenite. We propose a model involving the differential melting of a subduction-modified mantle source to account for the generation of these three suites of basalts. Asthenospheric mantle beneath the eastern NCC, which entrains garnet pyroxenite with an EM1 isotopic signature, was metasomatized by carbonatitic melts from carbonated eclogite derived from subducted Pacific slab materials present in the deeper mantle. High degree melting of garnet pyroxenites from a shallower mantle source produced the early (~23–20 Ma) higher-Si basalts. Mixing of these materials with deeper-sourced melts of carbonated mantle source produced the moderate-Si basalts. A thicker lithosphere after 9 Ma precluded melting of shallower garnet pyroxenites, so melts of the deeper carbonated mantle source are responsible for the low-Si basalts.

* Corresponding author. Tel.: +86 20 85290627; fax: +86 20 85291510.
E-mail address: hongyanli@gig.ac.cn (H.-Y. Li).

http://dx.doi.org/10.1016/j.gca.2015.12.032
0016-7037/

1. INTRODUCTION

Subduction of oceanic plates, and the associated dehydration, decarbonation and partial melting of subducted oceanic crust and sediments, will recycle crustal materials into the deep mantle, and can also feed volatiles into overlying mantle domains (e.g., Sleep and Zahnle, 2001; Dasgupta and Hirschmann, 2010; van Keken et al., 2011). These phenomena can together generate significant local heterogeneity in the mantle. As observed in the systematics of highly incompatible trace elements and in radiogenic isotopic systems, recycled crustal materials can become the enriched components in intraplate basalts (e.g., Zindler and Hart, 1986; Hofmann, 1997; Niu and O'Hara, 2003; Stracke et al., 2005; Willbold and Stracke, 2006; Ren et al., 2006, 2009).

A high-velocity feature representative of the stagnant subducted Pacific Plate in the mantle transition zone (MTZ, 410–660 km) beneath the eastern Eurasian continent has been imaged by P-wave tomography (e.g., Fukao et al., 1992; Zhao, 2004). Although there is consensus that subduction of the Pacific Plate had profound and lasting impacts on the tectonic and magmatic evolution of the eastern China (e.g., Sun et al., 2007; Zhu et al., 2012a, b), how the stagnant Pacific slab contributed to the overall compositional characteristics of intraplate basalts, specifically as to how its involvement may have influenced the alkaline character of these lavas (which range from quartz–normative to nepheline–normative) has not been explicitly addressed (e.g., Zhao et al., 2009; Kuritani et al., 2011; Tang et al., 2014). In eastern China, Cenozoic intraplate basalts occur primarily along its eastern continental margin (Fig. 1). This region constitutes an important part of the active volcanic belt of the western circum-Pacific rim (Zhou and Armstrong, 1982; Fan and Hooper, 1991; Xu et al., 2012a). The enriched components of Cenozoic basalts in eastern China are considered highly correlated to the subducted Pacific slab (Zhao et al., 2009; Kuritani et al., 2011; Xu et al., 2012a; Xu, 2014). For instance, the EM1 components of intracontinental basalts erupted in eastern China are interpreted to be related to dehydration of the subducted Pacific slab (e.g., Zhao et al., 2009; Kuritani et al., 2011), although alternative models have been proposed (e.g., Tang et al., 2014). It is important to note that the distribution of the enriched components of eastern China basalts delineates a strong provinciality (Fig. 1). The sources of northeastern China basalts have been described as mixing between an isotopically depleted mantle and EM1 mantle (e.g., Liu et al., 2008; Chen et al., 2009; Zeng et al., 2010; Kuang et al., 2012; Xu et al., 2012a,b; Hong et al., 2013; Li et al., 2014), while those of southeastern China basalts have been characterized as mixing between a depleted mantle and EM2 mantle (e.g., Zou et al., 2000; Huang et al., 2013). Therefore, it is unreasonable to simply attribute the enriched components of eastern China basalts to the stagnant Pacific slab in the MTZ.

Recycled crustal materials, i.e., oceanic crust and marine sediments, are geochemically enriched compared to depleted peridotitic mantle (e.g., Plank and Langmuir, 1998; Chauvel et al., 2008). When transported into the deep mantle, these crustal materials should metamorphose under eclogite facies conditions, and/or react with peridotite to form pyroxenite domains (e.g., Hauri, 1996; Sobolev et al., 2005, 2007; Straub et al., 2008; Herzberg, 2011). The chemical compositions and mineral assemblages of these mantle sources affect the chemistry of the melts. Thus, coherent relationships between the chemistry of host basalts (e.g., major-trace elements and Sr–Nd–Hf isotopes) and of minerals (e.g., Ni, Mn and Ca concentrations in olivine phenocryst) may be evident if recycled crustal materials contributed to the sources of these intraplate basalts. Here we report on the chemical compositions of melt inclusions, hosting olivines and bulk rocks of a suite of intraplate basalts, including tholeiites, alkali olivine basalts, basanites, and nephelinites, in western Shandong and Bohai Bay Basin of the eastern NCC, to assess the effects of the subducted Pacific slab on their chemical makeup.

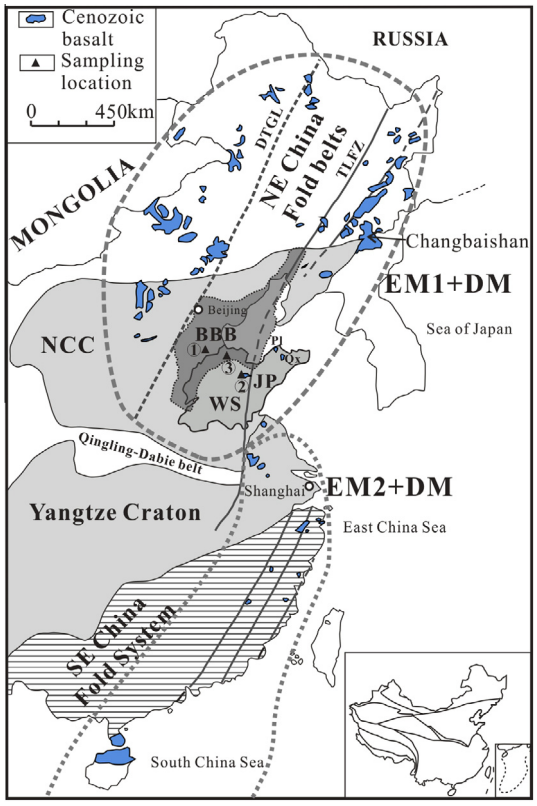

Fig. 1. Simplified geological map of the eastern China with distributions of Cenozoic basalts [modified from Xu et al. (2012a)]. Sample locations are marked in black triangles: ①, GG16-2; ②, Changwei depression; ③, Dashan of Wudi. NCC: North China Craton; BBB: Bohai Bay Basin; WS: Western Shandong; JP: Jiaodong Peninsula; DTGL: Daxinganling–Taihang Gravity Lineament; TLFZ: Tan-Lu Fault Zone; Pl: Penglai; Qx: Qixia. The distribution of mantle components in the source of Cenozoic basalts in eastern China is after Qin (2008) and Chen et al. (2009).

2. GEOLOGICAL SETTING AND SAMPLING

The NCC, located in the central part of eastern China, is one of the world's oldest cratons (~ 3.8 Ga; Liu et al.,

1992). Traditionally, the NCC is separated into two different tectonic domains by the near N-S trending Daxinganling-Taihangshan gravity lineament (DTGL), i.e., the eastern NCC and the western NCC (Fig. 1). Affected by subduction of the Pacific plate (e.g., Sun et al., 2007; Zhu et al., 2012a,b), the eastern NCC experienced significant decratonization during the late Mesozoic–Cenozoic, characterized by widespread intracontinental magmatism, faulting, and basin subsidence (e.g., Yang et al., 2008; Xu et al., 2009).

The Shandong Province is located in the southeast of the NCC, and is cut by the Tan-Lu Fault Zone (TLFZ) into two parts: the Jiaodong Peninsula and western Shandong. The Bohai Bay Basin (BBB), a Cenozoic rifted intraplate basin, is located in the central part of the eastern NCC and covers the northwestern part of the western Shandong (Fig. 1). Based on the relationships between faults and sedimentary sequences, the BBB experienced episodic rifting from the Middle Paleocene to the Late Oligocene coincident with regional extension of the eastern NCC. From Miocene to the present, the BBB subsided in a post-rift phase of thermal subsidence with primarily strike-slip faulting activity (Allen et al., 1997; Qi and Yang, 2010).

The Cenozoic basalts in the BBB and Shandong Province erupted largely during three periods. The earliest basalts, with $^{40}Ar/^{39}Ar$ ages of 46.9–45.5 Ma, are borehole samples of alkali basalt from the BBB (Li et al., 2014). The second eruptive period, 23.0–10.3 Ma is based both on borehole samples from the BBB (Li et al., 2014) and outcrops along the TLFZ (He et al., 2011; Xu et al., 2012b), comprising mostly alkali basalt and basanite. The last magmatic episode, 8.7–0.3 Ma, consists of scattered and isolated basaltic centers erupting mainly basanite and nephelinite, occurring as outcrops far from the TLFZ, such as Penglai and Qixia in the Jiaodong Peninsula and Wudi in the overlap region between the western Shandong and BBB (e.g., Zeng et al., 2010). Basalts from the latter two periods commonly contain mantle xenoliths (Chu et al., 2009; Liu et al., 2015).

We have sampled lavas from four volcanoes: Ergushan, Taohuashan, and Chenjiaguanzhuang, all from the Changwei depression along the TLFZ (~20 Ma; He et al., 2011; Xu et al., 2012b), as well as Dashan volcano of Wudi, in the overlap region between the western Shandong and BBB (<1 Ma; Luo et al., 2009). As well, we have obtained a lava sample from a borehole in the BBB (GG16-2; Fig. 1) with a bulk rock $^{40}Ar/^{39}Ar$ plateau age of ~23 Ma (Fig. S1). All the examined samples have minor olivine and clinopyroxene phenocrysts in a groundmass of olivine, plagioclase, clinopyroxene, Ti-magnetite, and glass.

Xenocrystic olivine is common in continental volcanic rocks, and is present in the Cenozoic basalts of the eastern NCC (e.g., Zeng et al., 2011; Sakuyama et al., 2013). Three populations of olivine are evident in the nephelinite from Dashan of Wudi, and can be recognized based on size, morphology and inclusions. The first population (I) are angular fragments with fluid inclusions in 'secondary' trails, but without original isolated melt inclusions (Fig. 2a). The second population (II) is characterized by euhedral crystal shapes, fluid inclusions, and isolated melt inclusions on grain margins (Fig. 2b–d). The grain sizes in populations I and II, both of which show maximum radii of ~1 mm, are consistently larger than the grain sizes in population III olivine (at ⩽0.3 mm). Population III olivines typically show euhedral and sub-euhedral grain shapes, with melt inclusions in their cores; and they may look cloudy due to abundant inclusions (Fig. 2e). The presence of three different populations of olivine in the nephelinite sample is similar to what has been encountered in kimberlites (e.g., Kamenetsky et al., 2008).

3. ANALYTICAL METHODS

3.1. Sample preparation

The basalt samples were initially sawn into slabs. After selecting billets for thin sections, the remaining pieces were crushed into small chips (~0.5 cm in maximum length), and a selection of fresh, aphyric chips were powdered for bulk rock analysis. Before powdering, the chips were leached with 1% HCl and washed with deionized water in an ultrasonic bath to remove the potential invisible calcite filling. The leached chips were then powdered to <200 mesh in a corundum mill for bulk rock analyses.

Based on our bulk rock results, three representative samples were chosen for detailed study of their olivines and olivine-hosted melt inclusion: a nephelinite sample with the lowest SiO_2 content (sample CZ), a tholeiite sample with the highest SiO_2 content (sample GG16-2), and a basanite sample with intermediate SiO_2 (sample YS13). Olivine grains were handpicked using a binocular microscope after crushing sample chips to 60–80 mesh.

3.2. Bulk rock analysis

All analyses were conducted in the State Key Laboratory of Isotope Geochemistry, Guangzhou Institute of Geochemistry, Chinese Academy of Sciences (GIGCAS).

Fusion beads of the basalt samples were prepared using a Rigaku desktop sample fusion system. Bulk-rock major element abundances were measured using a Rigaku RIX 2000 X-ray fluorescence spectrometer (XRF). Replicate analyses of standard W-2 point to precision (relative standard deviation expressed in percentage, RSD) better than ±0.6% for TiO_2 and better than ±0.3% for the other major oxides (Table 1), and accuracy (expressed in percentage) of better than ±2.0% for SiO_2, Al_2O_3, MgO, CaO and Na_2O, better than ±4.5% for TiO_2, $Fe_2O_3^T$, MnO and K_2O, and of ~±7% for P_2O_5 (at very low concentration: 0.13%) relative to accepted values. Trace element abundances were measured using a Perkin–Elmer Sciex ELAN 6000 quadrupole inductively coupled plasma mass spectrometer (ICP-MS), after acid digestions using HF-HNO_3 mixture in high-pressure Teflon vessels. Analytical precision for the rare earth elements (REE) and most of other incompatible elements is typically ±1–5%. A detailed description of the ICP-MS analytical methods can be found in Li et al. (2005).

Sample CZ from Dashan, borehole sample GG16-2, and half of the Changwei depression samples were selected for radiogenic isotope analysis (Table 2). For Sr–Nd–Hf

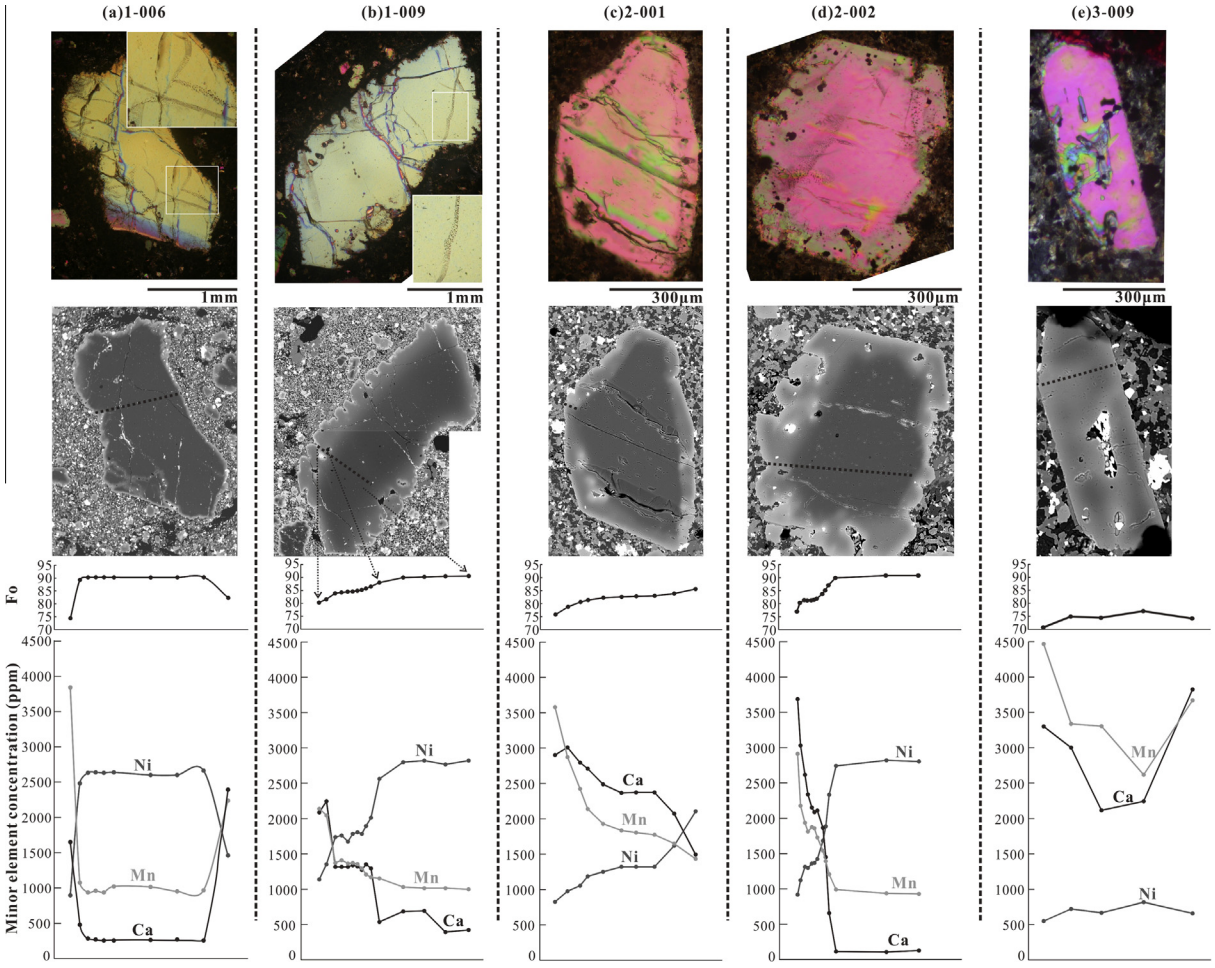

Fig. 2. Optical images (crossed-nicols, with partial enlarged image showing fluid inclusion), back-scattered electron images (with dotted electron probe microanalysis path) and chemical patterns for representative olivine crystals in nephelinite sample CZ from Dashan of Wudi. The black lines below the optical images are scale bars.

isotopic measurement, ~100 mg of powder was dissolved in an HF-HNO_3 mixture in a Teflon beaker at 150 °C for 7 days. High field-strength elements, Sr and the rare earths were separated by ion chromatography using AG50-X8 cation exchange resin. Separations of Nd and Hf were carried out on a HDEHP-coated Kef column (Li et al., 2014). Sr–Nd–Hf isotopic ratios were measured with a Neptune multicollector-ICPMS, and normalized to values for $^{86}Sr/^{88}Sr$ of 0.1194, $^{146}Nd/^{144}Nd$ of 0.7219 and $^{179}Hf/^{177}Hf$ of 0.7325, respectively. Sr, Nd, and Hf standards analyzed along with samples gave $^{87}Sr/^{86}Sr = 0.710269 \pm 7$ ($n = 6$) for NISTSRM987; $^{143}Nd/^{144}Nd = 0.512093 \pm 6$ ($n = 10$) for Shin Etsu JNdi-1; and $^{176}Hf/^{177}Hf = 0.282184 \pm 6$ ($n = 7$) for JMC14374 (the errors are given as SD). The USGS standard reference material BHVO-2 was used to monitor the ion-exchange chromatographic purification processes. One analysis of BHVO-2 gave $^{87}Sr/^{86}Sr = 0.703487 \pm 6$, $^{143}Nd/^{144}Nd = 0.512970 \pm 4$ and $^{176}Hf/^{177}Hf = 0.283099 \pm 4$ (the errors are given as 2 SE), respectively, in agreement with recommended values of $^{87}Sr/^{86}Sr = 0.703481 \pm 20$, $^{143}Nd/^{144}Nd = 0.512983 \pm 10$ and $^{176}Hf/^{177}Hf = 0.283096 \pm 20$ (Weis et al., 2005).

3.3. Olivine and melt inclusion analyses

Olivine melt inclusions were homogenized to eliminate post-crystallization effects, following procedures described by Ren et al. (2005). The olivine grains were reheated in a 1 atm gas mixing furnace with oxygen fugacity maintained at the quartz–fayalite–magnetite (QFM) buffer. After heating at 1250 °C for 10 min, olivines were quickly raised to the top of the furnace and quenched to produce homogeneous glass inclusions. The olivines were then mounted in epoxy resin disks and polished until the glassy inclusions were exposed.

Back-scattered electron (BSE) imaging and bulk chemical determinations of the olivines and their melt inclusions were conducted via electron probe microanalysis (EPMA) using a JEOL JXA-8100 Superprobe, following the procedures of Sobolev et al. (2007) for olivines, and of Wang and Gaetani (2008) for melt inclusions. The operating conditions for olivine analyses were a 20 kV accelerating voltage with a beam current of 300 nA and a 2 μm diameter, while for melt inclusion we used a 15 kV accelerating voltage with a beam current of 20 nA and a 3 μm diameter. Na

Table 1
Major and trace elemental compositions of basalts from western Shandong and BBB.

Sample	WF11	WF12	WF21	WF22	WF31	WF32	WF33	YS11	YS12	YS13	CZ	GG16-2	Standard rock		
Location	Changwei depression										Wudi	BBB	W-2	RSD (%)	Accepted value
	Ergushan				Taohuashan			Chenjiaguanzhuang			Dashan	Borehole GG16			
	E118°48′26″ N36°35′19″		E118°48′22″ N36°35′18″		E118°48′17″ N36°34′38″			E118°47′28″ N36°03′31″			E117°40′49.1″ N38°0′44.2″				
Major oxides (wt%)															
SiO_2	44.54	43.51	44.48	43.98	44.06	44.08	43.82	43.84	43.84	43.82	40.96	50.19	52.32	0.01	52.44
TiO_2	2.67	2.72	2.64	2.71	2.74	2.79	2.72	2.60	2.59	2.59	2.91	1.75	1.09	0.53	1.06
Al_2O_3	13.73	13.46	13.63	13.65	13.64	13.74	13.35	13.56	13.45	13.50	9.71	13.33	15.13	0.08	15.35
$Fe_2O_3^T$	12.45	12.52	12.35	12.51	12.38	12.42	12.45	13.18	13.18	13.19	16.06	11.15	10.32	0.11	10.74
MnO	0.17	0.18	0.17	0.18	0.17	0.17	0.17	0.18	0.18	0.18	0.23	0.13	0.17	0	0.16
MgO	10.87	10.30	11.10	10.42	11.06	10.82	11.60	10.10	10.28	10.05	11.93	8.77	6.34	0.16	6.37
CaO	9.87	9.70	9.63	9.92	9.22	9.42	9.13	9.82	9.75	9.64	10.02	9.17	10.68	0.05	10.87
Na_2O	3.17	4.03	2.77	2.49	3.05	3.22	3.03	3.17	3.40	3.36	4.39	2.62	2.16	0.27	2.14
K_2O	1.91	1.70	2.12	2.22	2.56	2.04	2.40	1.70	1.67	1.58	2.20	0.58	0.65	0	0.63
P_2O_5	0.66	0.67	0.61	0.69	0.64	0.65	0.62	0.75	0.74	0.74	1.01	0.27	0.14	0	0.13
LOI	0.59	1.34	0.73	1.42	0.80	0.86	1.00	1.40	1.03	0.87	0.19	1.64			
Total	100.63	100.13	100.23	100.19	100.32	100.21	100.29	100.30	100.11	99.52	99.60	99.60			
Trace elements (ppm)															
Sc	26.3	29.1	29.0	24.4	30.8	22.8	27.4	23.5	22.4	27.6	18.0	23.5	36.0	0.16	35.0
Cr	321	287	324	307	332	320	348	242	257	253	339	340	97	10.79	93
Co	56	55	59	54	55	53	56	53	55	56	102	54	44	0	44
Ni	257	223	252	236	258	254	257	215	227	220	295	201	72	1.39	70
Rb	22.3	20.8	26.3	24.9	29.7	23.9	27.1	18.6	18.7	18.0	32.2	4.3	20.1	4.01	20.0
Sr	702	732	697	770	693	699	649	964	827	877	1080	410	187	5.56	194
Y	22.1	20.8	20.7	22.1	20.0	20.2	19.4	20.1	20.1	19.3	30.3	17.4	20.8	6.76	23.0
Zr	217	214	201	220	243	236	234	250	247	240	354	120	92	3.13	94
Nb	57.0	56.8	52.6	60.1	63.1	63.5	58.9	64.0	63.0	63.2	122.9	18.9	6.5	2.34	7.8
Cs	0.20	0.33	0.25	0.27	0.28	0.30	0.27	0.21	0.20	0.18	0.55	0.08	0.93	3.30	0.99
Ba	389	385	371	394	375	367	348	294	292	305	481	217	168	3.06	173
La	42.1	41.7	37.5	44.1	37.7	38.3	36.6	42.0	42.7	42.9	70.9	15.8	10.6	4.11	10.0
Ce	78.8	78.0	74.2	80.9	74.2	73.4	68.4	82.3	83.8	81.3	133.8	33.0	23.0	2.96	23.5
Pr	9.66	9.79	8.71	9.84	9.06	9.25	8.83	9.94	10.11	10.28	15.98	4.30	3.08	2.60	3.20
Nd	38.8	37.6	36.0	39.3	36.2	37.3	33.4	41.0	41.9	39.3	63.5	18.5	13.2	0.76	14.0
Sm	7.78	7.51	7.28	7.64	7.27	6.97	7.11	7.93	8.14	8.05	12.61	4.51	3.28	2.11	3.25
Eu	2.66	2.38	2.43	2.57	2.40	2.42	2.28	2.51	2.62	2.59	3.87	1.61	1.09	4.85	1.01
Gd	6.97	7.10	6.86	7.00	6.77	6.47	6.22	6.71	6.85	7.20	11.08	4.64	3.66	0.95	3.60
Tb	1.07	0.97	1.02	1.02	0.98	0.95	0.92	0.96	1.03	0.93	1.47	0.70	0.62	2.45	0.63
Dy	5.58	5.48	5.24	5.42	5.22	4.99	5.02	5.08	5.21	5.08	7.22	3.90	3.93	0.29	3.80
Ho	1.03	0.95	0.95	1.02	0.92	0.92	0.86	0.88	0.89	0.90	1.23	0.75	0.84	1.38	0.76
Er	2.53	2.32	2.38	2.46	2.41	2.25	2.11	2.23	2.03	2.14	2.73	1.76	2.21	1.04	2.40
Tm	0.34	0.33	0.32	0.33	0.31	0.29	0.28	0.26	0.27	0.27	0.32	0.24	0.32	0	0.38
Yb	1.88	1.78	1.95	1.95	1.73	1.75	1.59	1.58	1.58	1.56	1.77	1.43	2.03	1.03	2.05

(*continued on next page*)

Table 1 (*continued*)

Sample	WF11	WF12	WF21	WF22	WF31	WF32	WF33	YS11	YS12	YS13	CZ	GG16-2	Standard rock		
Location	Changwei depression										Wudi	BBB	W-2	RSD (%)	Accepted value
	Ergushan				Taohuashan			Chenjiaguanzhuang			Dashan	Borehole GG16			
	E118°48′26″ N36°35′19″		E118°48′22″ N36°35′18″		E118°48′17″ N36°34′38″			E118°47′28″ N36°03′31″			E117°40′49.1″ N38°0′44.2″				
Lu	0.29	0.29	0.26	0.29	0.26	0.25	0.24	0.23	0.22	0.22	0.24	0.20	0.31	3.23	0.33
Hf	4.79	4.47	4.47	5.08	4.90	5.12	4.85	5.33	5.10	5.08	7.65	3.13	2.40	1.74	2.40
Ta	3.56	3.64	3.43	3.94	4.22	4.16	3.94	4.00	4.05	4.11	7.02	1.30	0.47	3.27	0.50
Pb	5.56	5.77	6.34	5.46	6.54	6.67	5.17	5.02	4.67	4.77	4.24	2.01	7.48	6.52	8.77
Th	4.97	4.74	4.51	5.05	4.89	4.97	4.64	4.87	4.92	4.85	9.65	1.94	2.21	0.26	2.20
U	1.50	1.54	1.36	1.59	1.59	1.54	1.49	1.63	1.56	1.58	2.80	0.40	0.50	1.15	0.53
K_2O/TiO_2	0.72	0.63	0.80	0.82	0.93	0.73	0.88	0.65	0.64	0.61	0.76	0.72			
Th/Nb	0.09	0.08	0.09	0.08	0.08	0.08	0.08	0.08	0.08	0.08	0.08	0.10			
La/Yb	22.39	23.43	19.23	22.62	21.79	21.89	23.02	26.58	27.03	27.50	40.05	11.05			
Sm/Yb	4.14	4.22	3.73	3.92	4.20	3.98	4.47	5.02	5.15	5.16	7.12	3.15			
Ba/Th	78.27	81.22	82.26	78.02	76.69	73.84	75.00	60.37	59.35	62.89	49.84	111.86			
Ce/Pb	14.17	13.52	11.70	14.82	11.35	11.00	13.23	16.39	17.94	17.04	31.59	16.42			

$Fe_2O_3^T$ is total iron as Fe_2O_3.

and K were measured first for each melt inclusion analysis, using 10 s peak counting time and 5 s background counting time on both sides to minimize their possible loss during analysis. An internal olivine and glass standard JB-2 were analyzed with the samples to monitor the machine drift. The relative analytical uncertainty (RSD, relative standard deviation) for the internal olivine standard is better than 1.7% for major elements (SiO_2, MgO and FeO), and 2.2–3.2% for minor elements (CaO, MnO and NiO; Supplemental Table S2), and for glass standard JB-2 is better than 0.4% for most major elements (11.8%, 1.2% and 11.4% for MnO, K_2O and P_2O_5, respectively). The analyses of glass standard JB-2 give Na_2O ($2.04 \pm 0.007\%$) and K_2O ($0.42 \pm 0.005\%$) concentrations in agreement with recommended values ($Na_2O = 2.04 \pm 0.026\%$, $K_2O = 0.42 \pm 0.011\%$; Supplemental Table S3), indicating that Na and K loss is insignificant during our analyses. To investigate the chemical composition of different kinds of olivine in the low-Si samples, *in situ* analyses of olivines in thin section were also carried out following the methods described above.

4. RESULTS

4.1. Bulk rock chemical composition

Bulk rock major-trace element and Sr–Hf–Nd isotope results are presented in Table 1 and Table 2, respectively, and are shown in Figs. 3–5 in the context of results from Zeng et al. (2010, 2011). The bulk chemical compositions of basalts from western Shandong and Bohai Bay Basin (BBB) vary systematically with their SiO_2 concentration. Therefore, the samples analyzed in this study, together with samples of Zeng et al. (2010, 2011) are divided into three groups according to their bulk rock SiO_2 concentrations (Fig. 3): (1) high-Si lavas, comprising tholeiites, alkaline basalts and trachybasalts; (2) moderate-Si lavas, mainly basanites; and (3) low-Si lavas, which include transitional basanites and nephelinites.

The high-Si samples have lower alkalies, CaO and FeO^T contents than the low-Si samples. The alkalies, CaO and FeO^T contents, and the ε_{Nd} values of the basalts all show a roughly negative correlation with SiO_2 content (Fig. 3). All the basalts in western Shandong and BBB display OIB-like geochemical features, i.e., enrichment of most of the incompatible elements (e.g., Ba, Rb, Cs, U, and Sr) with positive Nb–Ta anomalies (Fig. 4a). The high-Si samples have lower trace element concentrations and less fractionated rare earth elements (REEs) (La/Yb = 11.1–25.0; Sm/Yb = 3.2–4.8) than either the moderate-Si samples (La/Yb = 16.3–33.3; Sm/Yb = 3.8–6.0) or the low-Si samples (La/Yb = 40.1–43.2; Sm/Yb = 7.1–7.6) (Fig. 4b). The high-Si samples show enrichments in the more fluid-mobile elements (e.g., Ba and Sr; Fig. 4a) on primitive-mantle normalized multi-element plots, and are characterized by higher Ba/Th and lower Ce/Pb than the low-Si samples (Fig. 4c and d). The high-, moderate- and low-Si basalts have K_2O/TiO_2 ratios of 0.33–0.96, 0.30–0.93 and 0.76–0.84, respectively, and show no correlations with their SiO_2 contents. All the basalts fall within a narrow

Table 2
Sr-Nd-Hf isotopic compositions of basalts from western Shandong and BBB.

Sample	WF12	WF22	WF32	YS11	YS13	CZ	GG16-2
$^{87}Sr/^{86}Sr$	0.703282	0.703353	0.703306	0.703918	0.703688	0.703611	0.704330
2SE	0.000008	0.000007	0.000007	0.000006	0.000006	0.000008	0.000006
$^{143}Nd/^{144}Nd$	0.512906	0.512912	0.512903	0.512901	0.512899	0.512939	0.512663
2SE	0.000003	0.000004	0.000003	0.000004	0.000003	0.000004	0.000004
ε_{Nd}	5.23	5.34	5.17	5.12	5.09	5.87	0.50
$^{176}Hf/^{177}Hf$	0.282998	0.282984	0.282990	0.282999	0.282996	0.283018	0.282870
2SE	0.000003	0.000004	0.000003	0.000002	0.000003	0.000002	0.000004
ε_{Hf}	7.99	7.49	7.72	8.03	7.92	8.70	3.47

SE: standard error; $\varepsilon_{Nd} = [(^{143}Nd/^{144}Nd)_{sample}/(^{143}Nd/^{144}Nd)_{CHUR}\text{-}1] \times 10^4$, where $(^{143}Nd/^{144}Nd)_{CHUR} = 0.512638$ (Jacobsen and Wasserburg, 1980); $\varepsilon_{Hf} = [(^{176}Hf/^{177}Hf)_{sample}/(^{176}Hf/^{177}Hf)_{CHUR}\text{-}1] \times 10^4$, where $(^{176}Hf/^{177}Hf)_{CHUR} = 0.282772$ (Blichert-Toft and Albarède, 1997).

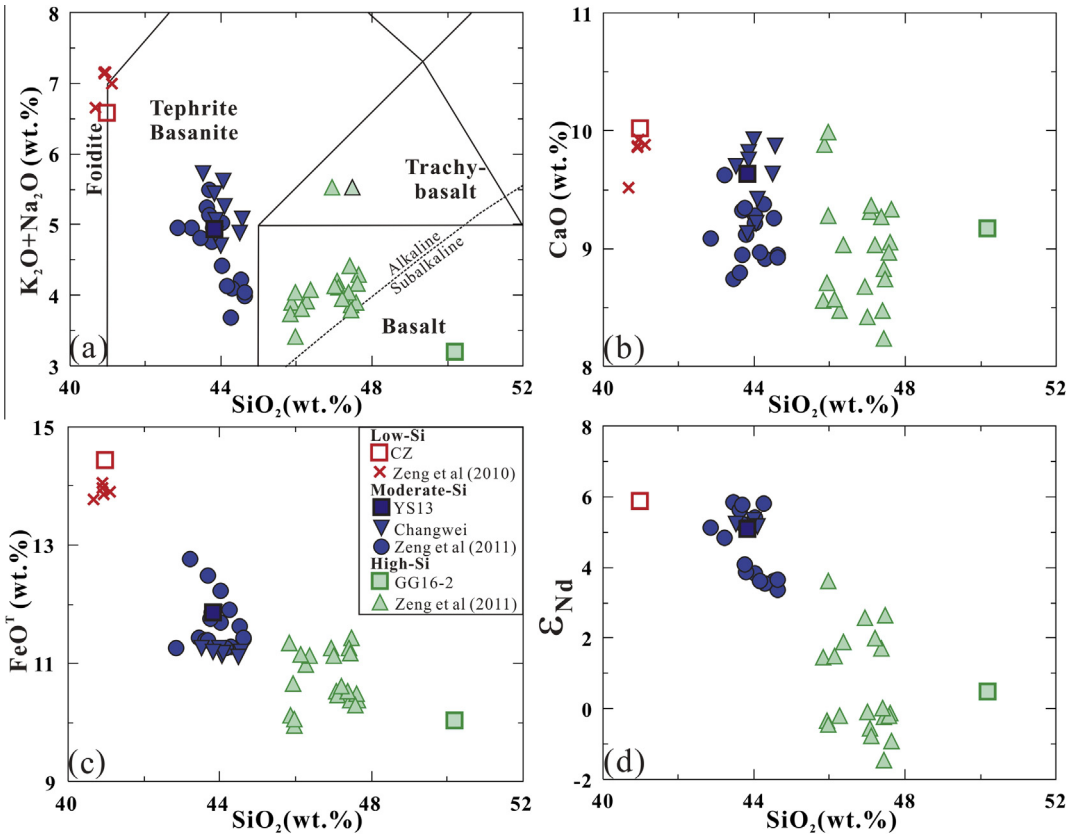

Fig. 3. Alkali content (a), CaO (b), FeO^T (c) and ε_{Nd} (d) versus SiO_2 diagrams for bulk rocks of basalts from western Shandong and Bohai Bay Basin. $FeO^T = 0.8998*Fe_2O_3^T$. The data of Zeng et al. (2010, 2011) are presented in Table S1.

range of Th/Nb ratios between 0.06 and 0.10 (Tables 1 and S1).

All the examined basalts fall between EM1 and depleted mantle sources in terms of their Sr–Nd isotopes. The high-Si basalts have slightly higher $^{87}Sr/^{86}Sr$ but lower ε_{Nd} than the low-Si samples (Fig. 5a). A notable characteristic of the Cenozoic basalts in the western Shandong and BBB is that their Hf and Nd isotopes fall along a mixing trend between the high- and low-Si sample endmembers (Chen et al., 2009; Zeng et al., 2011; Li et al., 2014), with the high-Si samples falling within the Indian Ocean mantle domain, and the low-Si samples falling within the Pacific Ocean domain, as per Pearce et al. (1999) (Fig. 5b and c). The chemical composition of all the western Shandong and BBB basalts can be explained via mixing trends between two end members in terms of major-trace elements and isotopes (Figs. 3–5).

4.2. Olivine and melt inclusion compositions

The chemical composition of olivines and their hosted melt inclusions are listed in Supplemental Tables S2 and S3, respectively. The measured data for the olivine-hosted melt inclusions have been corrected to account for the

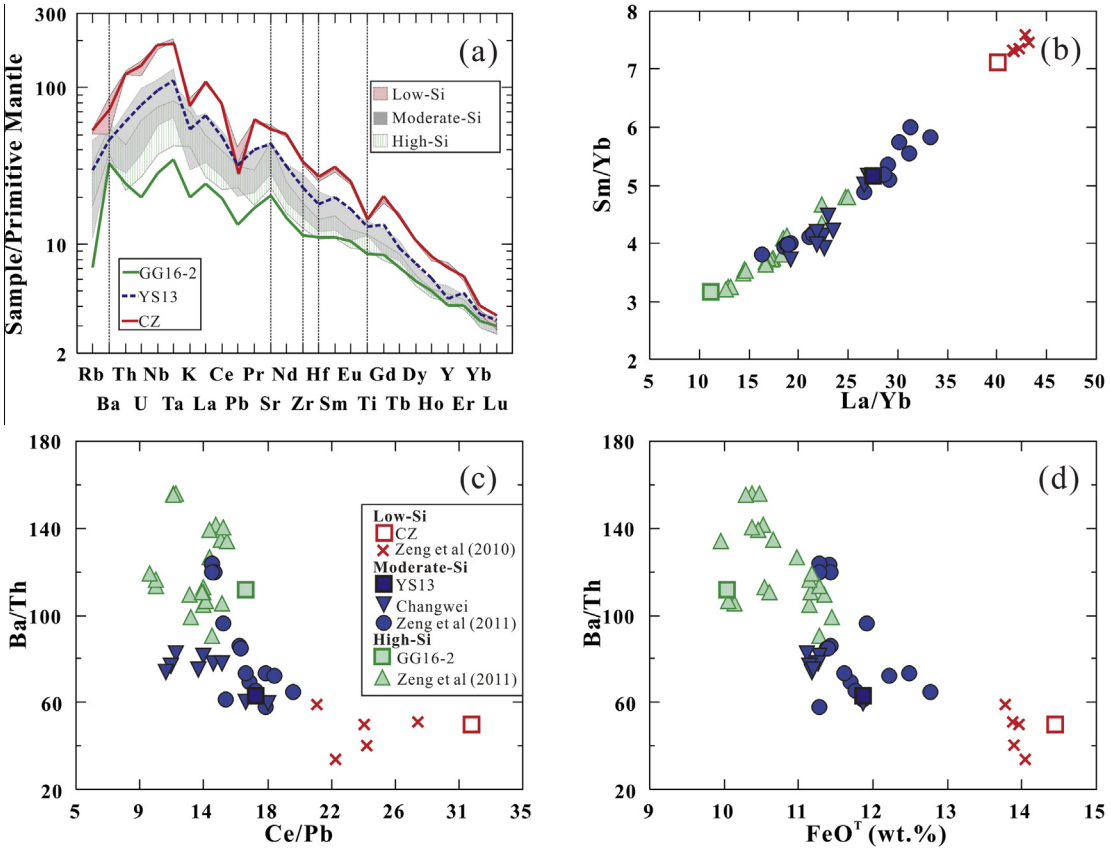

Fig. 4. Primitive mantle (McDonough and Sun, 1995) normalized trace element patterns (a), and Sm/Yb versus La/Yb (b), Ba/Th versus Ce/Pb (c), and Ba/Th versus FeO^T (d) correlations for basalts from western Shandong and Bohai Bay Basin. In diagram (a), the low-, moderate- and high-Si samples of Zeng et al. (2010, 2011) and this study are plotted in groups, respectively, while the three representative samples are plotted separately.

"Fe-loss" and recalculated to be in equilibrium with its host olivine, utilizing Petrolog3 software (Danyushevsky and Plechov, 2011) which applies the method of Danyushevsky et al. (2000) using the olivine–melt equilibrium model of Ford et al. (1983), with oxygen fugacity at the QFM buffer, typical of intraplate basaltic lavas (Carmichael and Ghiorso, 1986). In the recalculation, the FeO^T (total FeO) for the initial trapped melt was estimated to be similar to the FeO^T of the hosting bulk rock.

Sample GG16-2, YS13 and CZ contain olivines with Fo [defined as Fo = Mg/(Mg + Fe), where Mg and Fe are molar concentrations] contents of 72.3–86.1, 81.3–86.2, and 70.9–91.8, respectively, suggesting that the magmas involve mixtures of different components at several points along their liquid lines of descent. Ni contents and Fo values show a positive correlation, and Mn contents and Fo values are inversely correlated in olivines from the three samples. Olivines in the low-Si sample CZ are Ni-deficient but Mn-rich relative to olivines in the high-Si sample GG16-2 at a given Fo value (Fig. 6a and b). The olivines in the moderate-Si sample YS13 have Ni and Mn contents between the ranges of low-Si sample CZ and high-Si sample GG16-2 at a given Fo value. Olivines from GG16-2 have nearly constant Ca contents, while Ca and Fo values correlate inversely in the olivines from samples CZ and YS13 (Fig. 6c).

The olivine-hosted melt inclusions within individual samples record a wide range of MgO contents, supporting the contention that their hosting magmas are a mixture of components interacting at different stages during their evolution. The melt inclusions from the high-Si sample GG16-2 have higher SiO_2 and Al_2O_3 but lower CaO and TiO_2 contents at given MgO than inclusions from the low-Si sample CZ (Fig. 7). The melt inclusions from the moderate-Si sample YS13 have the SiO_2, Al_2O_3, CaO and TiO_2 contents between the ranges of the high- and low-Si sample. The CaO, Al_2O_3 and TiO_2 abundances in the melt inclusions of sample CZ are negatively correlated with their MgO contents, while their SiO_2 is nearly constant (Fig. 7). Weak negative correlations between CaO, Al_2O_3, TiO_2 and MgO for melt inclusions of sample GG16-2 are also observed. The melt inclusions within sample CZ, YS13 and GG16-2 have K_2O/TiO_2 ratios of 0.43∼0.80, 0.23∼0.92, and 0.10∼0.62, respectively.

5. DISCUSSION

5.1. Olivine phenocrysts or xenocrysts?

The angular shapes with kink-banded extinction patterns in population I olivine (Fig. 2a) in CZ suggests that they may be xenocrysts (Schiano, 2003). EMPA analyses

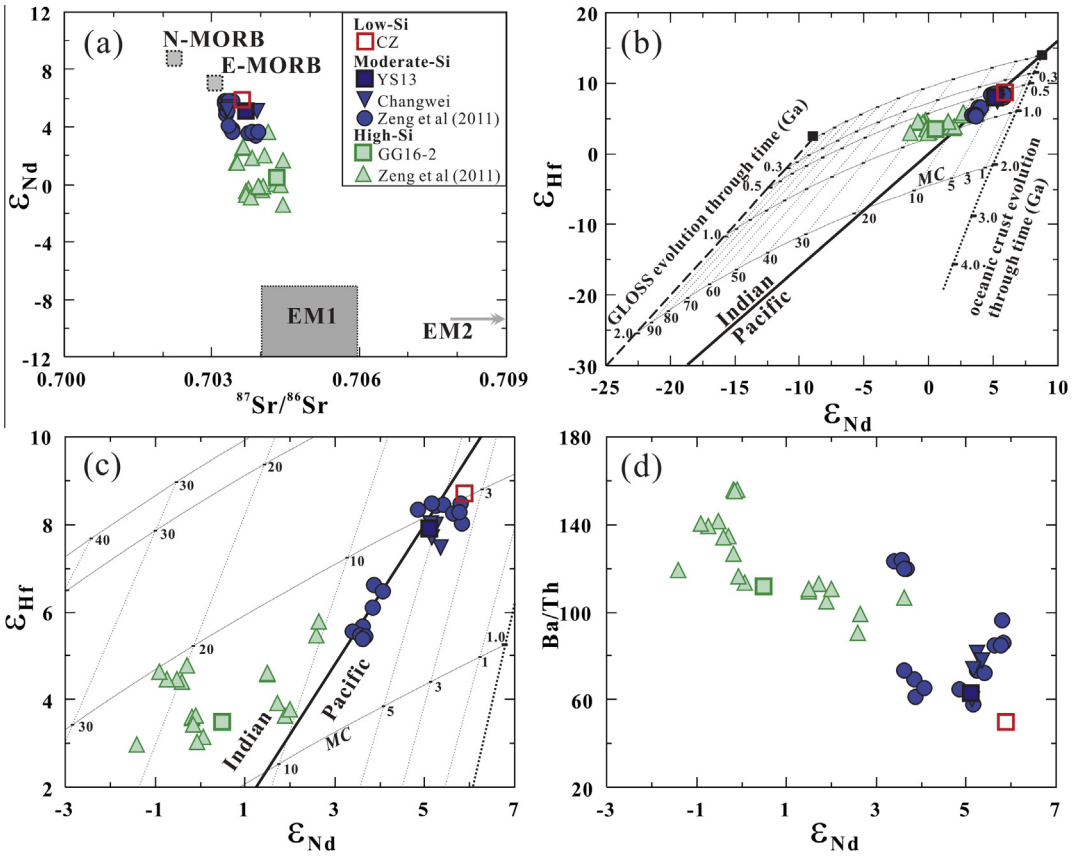

Fig. 5. ε_{Nd} versus $^{87}Sr/^{86}Sr$ (a), ε_{Hf} versus ε_{Nd} (b, c) and Ba/Th versus ε_{Nd} (d) correlation for basalts from western Shandong and Bohai Bay Basin. The Sr-Nd isotope signatures of N-MORB and E-MORB in diagram (a) are according Su and Langmuir (2003). The present-day average Nd–Hf isotopic compositions of MORB (Chauvel et al., 2008) and Global Subducted Sediment (GLOSS) (Plank and Langmuir, 1998; Chauvel et al., 2008) are also shown in the diagrams (b). The evolution paths of oceanic crust and GLOSS in (b) and (c) are calculated according the method of Chauvel et al. (2008), shown as dotted and dashed curves, respectively, marked by the ages (Ga). Mixing curves (MC) between GLOSS and oceanic crust were marked by the GLOSS proportions in percentage. The solid line in (b) and (c) is the boundary of Hf–Nd isotopic composition between the Indian and Pacific Ocean mantle domains (Pearce et al., 1999).

reveal that these angular olivine fragments have homogeneous chemical compositions aside from a narrow rim, consistent with their BSE images. Their cores have higher Fo values (>90) and Ni contents (>2600 ppm), lower Ca (<300 ppm) and Mn (<1100 ppm) than their margins (Fig. 2a). These olivines strongly resemble olivines from mantle xenoliths in Dashan and Changwei depression basalts (mostly with Fo > 89 and Ca < 715 ppm; Chu et al., 2009; Liu et al., 2015). BSE images show that the population II olivines in CZ typically have mantled cores (Fig. 2b–d). The cores have homogeneous chemical compositions resembling the population I olivine xenocrysts, while their mantles show decreasing Fo value and Ni, and increasing Mn and Ca. The mantles of population II olivines usually have ranges preserving nearly invariant chemical compositions (Fig. 2b–d). This phenomenon suggests that some olivine xenocrysts in CZ had developed overgrowths. Clear correlations are not observed between Ca contents and Fo values for xenocrystic cores, though there are positive correlations between Ni and Fo, and negative correlations between Mn and Fo. The magmatic olivines and the rims on xenocrystic cores show similar relationships among Ni, Mn, Ca and Fo value (Fig. 6). Mantling olivine in equilibrium with its host lava should have Ca > 1270 ppm, Mn > 1290 ppm and Ni < 1810 ppm (Fig. 6). Population III olivines, with euhedral shapes and relatively homogeneous BSE images suggesting they are magmatic origin, are chemically similar to the mantles of Type II olivines, save that their Ca and Mn contents show greater variation (Fig. 2e).

The olivines in the moderate-Si sample YS13 show correlations between Fo and Ca similar to those in the low-Si sample (Fig. 6c), suggesting that olivine xenocrysts with overgrowths are also present in the moderate-Si basalts. The olivine crystals in GG16-2 show euhedral and subhedral shapes that differ from xenocrystic grains (e.g., Kamenetsky et al. 2006). All the olivines in GG16-2 have Fo values lower than 89, lower limit of Fo for olivines from eastern NCC mantle xenoliths (e.g., Chu et al., 2009; Liu et al., 2015), which strongly suggests these olivines are cognate phenocrysts.

5.2. Contamination and fractional crystallization

Crustal contamination can affect mantle-derived melts during their ascent through the crust and their evolution

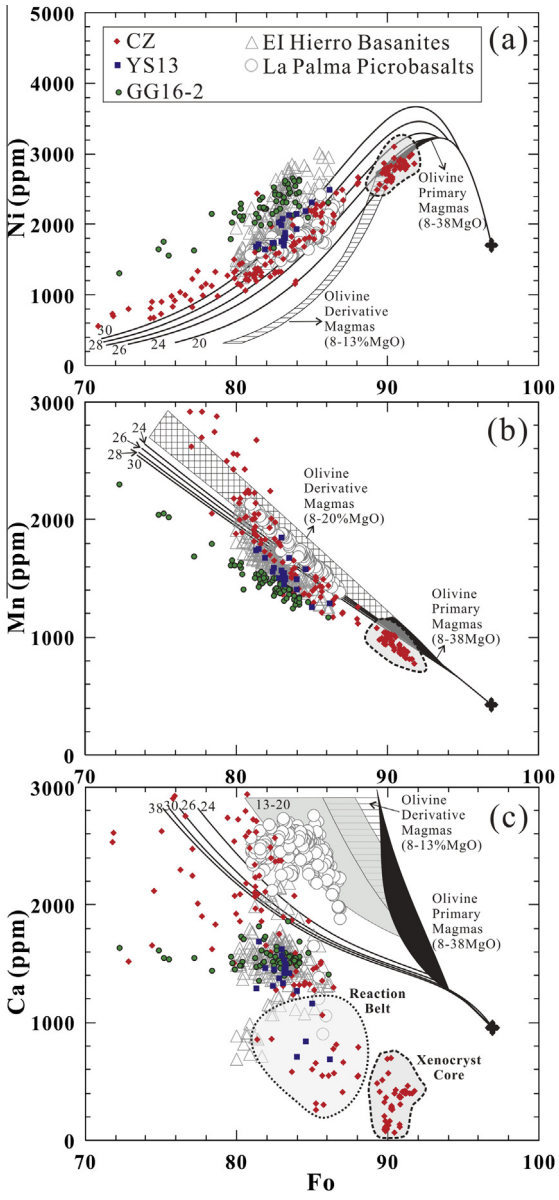

Fig. 6. Plots of Ni (a), Mn (b) and Ca (c) against Fo for olivines of basalts from western Shandong and Bohai Bay Basin. The olivines in sample CZ are distinguished as xenocryst (or core), magmatic mantle or crystal, with reaction belt between the xenocryst core and magmatic mantle. The data for EI Hierro basanites and La Palma picrobasalts are from the Canary Islands, Spain (Gurenko et al., 2009). The corresponding compositions of olivines crystallized from peridotite melts calculated by Herzberg (2011) are also shown. The calculation was based on a fertile peridotite source containing 1964 ppm Ni, 24,657 ppm Ca and 1007 ppm Mn. The calculated olivines are for both primary magmas and derivative liquids produced by olivine fractionation. The filled black fields are for calculated olivines of the primary magmas, the other numbered lines and fields are for calculated olivines from derivative liquids of primary magmas with different MgO concentration (Herzberg, 2011).

within magma chambers in continental environments. Because continental crust has a higher Th/Nb (0.70, Rudnick and Gao, 2003) than OIBs (0.08, Sun and McDonough, 1989), a negative correlation between Th/Nb and ε_{Nd} values would be predicted if crustal contamination played an important role in basalt petrogenesis. However, the intraplate basalts of this study have nearly constant Th/Nb ratios (0.06–0.1), and ε_{Nd} from −1.4 to +5.9 (Tables 1 and S1), which together with their peridotite xenocryst-bearing charcteristics (Chu et al., 2009; Liu et al., 2015), rule out crustal contamination as a significant cause of geochemical differences among our samples.

The melt inclusions in the high-Si sample GG16-2 are lower in TiO_2 (1.0–2.7%) and K_2O/TiO_2 (0.1–0.6) than the low-Si sample (TiO_2 of 2.8–3.9%; K_2O/TiO_2 of 0.4−0.8) (Table S3). The average upper and middle continental crust have TiO_2 content of 0.64% and 0.69%, respectively; and K_2O/TiO_2 ratios of 4.4 and 3.3, respectively (Rudnick and Gao, 2003). Therefore, the high-Si melts cannot be generated via contamination of lower-Si melts by the upper or middle continental crust materials, as this would result in lower TiO_2 but higher K_2O/TiO_2 ratios. Although the lower continental crust has lower TiO_2 content (0.82%, Rudnick and Gao, 2003) than the melt inclusions of this study, its K_2O/TiO_2 ratio (0.74, Rudnick and Gao, 2003) is higher than melt inclusions in the high-Si sample GG16-2 (0.1–0.6). Therefore, contamination of low-Si melts by the lower crust will not generate the high-Si melts, which have lower K_2O/TiO_2 ratios. These observations argue against crustal contamination strongly impacting the chemical compositions of our melt inclusions. The inverse correlations observed between the alkalies, CaO, FeO^T, ε_{Nd} and SiO_2 among the basalts in this study reflect the mixing of two endmember melts, little affected by fractional crystallization.

The CaO, Al_2O_3 and TiO_2 contents of the melt inclusions within individual sample of CZ and GG16-2 correlate inversely with MgO (Fig. 7), suggesting these samples experienced fractional crystallization of olivine, irrespective of their SiO_2 levels. However, fractional crystallization of clinopyroxene appears to have been insignificant, as there is no obvious drop of CaO with decreasing MgO for inclusions from any individual sample (Fig. 7). The well preserved negative correlation between alkali content, ε_{Nd} and SiO_2 for bulk rocks of this study further suggests that these basalts were little affected by fractional crystallization of olivine or other mineral phases, or their clear mixing trends would be obscured. As well, olivine has extremely low partition coefficients for the rare earths and other incompatible elements (e.g., McKenzie and O'Nions, 1991). Thus the trace element signatures of the high- and low-Si samples largely reflect their primary melts, with little influence by fractional crystallization. Therefore, the geochemical characteristics of the studied basalts largely reflect their mantle sources.

The chemical compositions of melt inclusions in the moderate-Si sample YS13 straddle those of the low-Si sample CZ and the high-Si sample GG16-2 (Fig. 7), suggesting that the moderate-Si basalts could be mixtures of the high- and low- Si basaltic melts. The trace element and isotopic signatures of the moderate-Si samples are consistent with such a model, i.e., intermediate trace elements concentrations, Sm/Yb, La/Yb, Ba/Th, Ce/Pb ratios (Fig. 4) and intermediate ε_{Nd} and ε_{Hf} (Fig. 5).

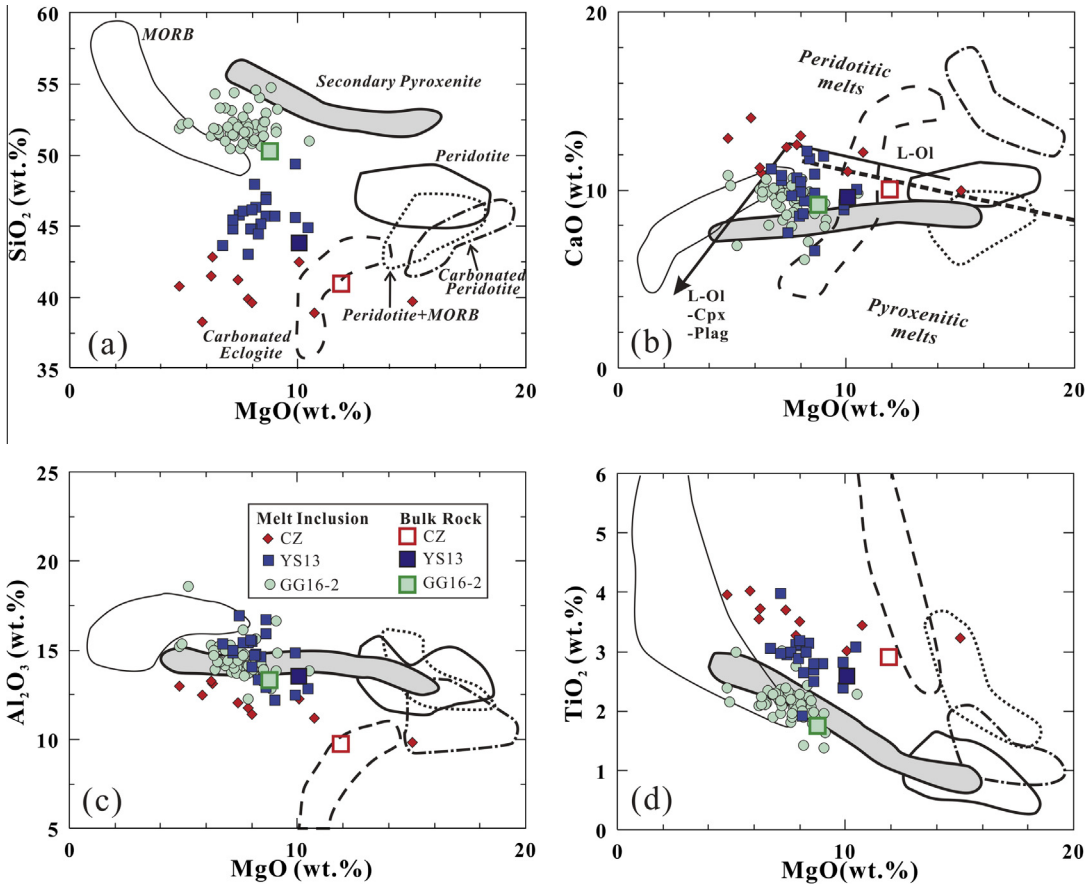

Fig. 7. Comparison of olivine melt inclusions of basalts from western Shandong and Bohai Bay Basin with high-pressure experimental melts of various starting materials. (a) SiO_2 versus MgO, (b) CaO versus MgO, (c) Al_2O_3 versus MgO, (d) TiO_2 versus MgO. Pressure, starting materials and data source: MORB: 2.0–3.0 GPa, G2 (MORB-like ecologite; Pertermann and Hirschmann, 2003); Secondary Pyroxenite: 3.5 GPa, Px-1 (Sobolev et al., 2007); Carbonated Eclogite: 3.0 GPa, SLEC1 + 5.0 wt% CO_2 (Dasgupta et al., 2006); Peridotite: 2.5–3.0 GPa, HK-66 and KLB-1 (Hirose and Kushiro, 1993); Carbonated Peridotite: 3.0 GPa, KLB-1 + 1.0 wt% CO_2 (Dasgupta et al., 2007); Peridotite + MORB: 3.0 GPa, KLB-1 + MORB (Kogiso et al., 1998). The halving line (CaO = 13.81–0.274MgO) in (b) between peridotitic and pyroxenitic melts is from Herzberg and Asimow (2008), with CaO higher and lower than the halving line are potential peridotitic and pyroxenitic melts, respectively.

5.3. A two-component mantle source

As discussed above, the chemical diversity of the basalts from western Shandong and Bohai Bay Basin cannot result from crustal contamination, or crystallization of a magma from a single mantle source. The basalts should have the isotopic signature of the mantle xenoliths if derived from the subcontinental lithospheric mantle, as is the case for isotopically enriched basalts in eastern Australia (O'Reilly and Zhang, 1995). The associated mantle xenoliths have more depleted Hf–Nd isotopes ($\varepsilon_{Nd} = 3.1$–24.0; $\varepsilon_{Hf} = 7.4$–655; Chu et al., 2009) than the hosting Cenozoic basalts in Shandong ($\varepsilon_{Nd} = -1.4$ to 5.9; $\varepsilon_{Hf} = 3.0$ to 8.7), which had been observed by Zeng et al. (2010). This precludes the possibility of lithospheric mantle as major source component for basalts of this study. Therefore, the observed bulk chemical variations must relate to varying contributions from enriched and depleted source components in the asthenospheric mantle.

Recycled oceanic crust, with or without sediments, is considered by many workers to be a probable endmember component in the mantle sources of OIBs (e.g., White and Hofmann, 1982; Hofmann, 1997; Chauvel et al., 2008), and these models have been used to explain the variable Sr–Nd–Hf–Pb isotope signatures in Cenozoic intracontinental basalts in eastern China (e.g., Xu et al., 2012a; Sakuyama et al., 2013; Li et al., 2014; Xu, 2014). However, an actual physical model for this mixing of source components has not yet been constrained. The contribution of recycled oceanic crust to the generation of intraplate basalts had been investigated experimentally. High pressure partial melts of quartz and coesite eclogites (Stage I eclogite, approximating average oceanic crust at high pressures; Green and Ringwood, 1967; Pertermann and Hirschmann, 2003) are silica-oversaturated and MgO-deficient compared to the basalts in this study, and thus cannot be their direct source (Fig. 7). Reactions between melts from these eclogites and peridotite (Sobolev et al.,

2005, 2007), or solid-state reactions between eclogite and peridotite (Herzberg, 2011) will form secondary pyroxenite. Sobolev et al. (2005, 2007) has emphasized the role of olivine-free pyroxenite on the generation of OIBs. In this study, pyroxenite is distinguished from peridotite by low olivine proportions [olivine/(olivine + orthopyroxene + clinopyroxene) < 0.4], per Streckeisen (1976), with garnet pyroxenites including variable percentages of garnet. As Ni is more compatible in olivine, while Mn and Ca preferentially partition into ortho- and clinopyroxene and garnet (Hart and Davis, 1978; Kinzler et al., 1990; Beattie et al., 1991; Herzberg, 2006; Herzberg and Asimow, 2008; Balta et al., 2011), the $D_{Ni}^{bulk/melts}$ of the secondary pyroxenite will be lower, while its $D_{Ca}^{bulk/melts}$ and $D_{Mn}^{bulk/melts}$ will be higher than that of peridotite. Melts that are higher in Ni and lower in Ca and Mn would be produced via secondary pyroxenite melting, and olivine would crystallize as a result (Sobolev et al., 2005; Herzberg, 2006, 2011; Hong et al., 2013). Therefore, coherent relationships between the chemical compositions of olivine phenocrysts (as expressed in their Ni, Mn and Ca concentrations) and their host rocks (seen via radiogenic isotopes) in intraplate basalts should be observed if secondary pyroxenite is involved (Sobolev et al., 2008). These relationships have been observed in OIBs from the Canary islands (Gurenko et al., 2009), in which the Ni, Mn and Ca concentrations in olivine show correlations with Sr, Nd and Pb isotopic ratios of their host rocks.

A temperature control model (e.g., Putirka et al. 2011), in which a single mantle source generates the whole spectrum of lavas, does not account for the isotopic differences observed in our studied samples. The differences in the chemistries of melt inclusions (Fig. 7), their hosting olivines (Fig. 6), and the bulk rock chemistries of the host basalts in this study suggest they developed from primary magmas derived from heterogeneous sources. Below, we focus on the petrogenesis of our high- and low-Si basalts. This examination is mostly based on comparisons of observed olivine chemistries with modeled olivine compositions crystallized from peridotite melts (Herzberg, 2011), and comparisons of chemistries between olivine melt inclusions and melts of various starting materials at ~3.0 GPa, a pressure can represent the circumstance at the top of the asthenosphere beneath the eastern NCC (Chen, 2010).

5.3.1. Garnet pyroxenite sources for the high-Si basalts

Chemistry of the olivines represents their corresponding melt. Higher Ni but lower Mn in olivines from the high-Si sample GG16-2 than that of the low-Si sample CZ at given Fo value (Fig. 6a and b) suggest that primitive melts of the high-Si samples are richer in Ni but poorer in Mn than those in the low-Si samples. If the chemical compositions of the melt inclusions were affected by fractional crystallization of an olivine dominated assemblage, the primary magma for the high-Si sample GG16-2 would be rich in Al_2O_3, but deficient in CaO and TiO_2 as compared with that of the low-Si sample CZ (Fig. 7).

Olivines in GG16-2 have higher Ni and lower Mn and Ca at a given Fo value than olivines from melts of mantle peridotite: they show similarities to the olivines in EI Hierro basanites, which have been explained as being derived from a pyroxene-rich source (Fig. 6; Gurenko et al., 2009; Herzberg, 2011). The melt inclusions in GG16-2 have SiO_2 contents that span the range between melts generated from material of MORB and secondary pyroxenite, but the primitive inclusions have MgO contents higher than can be generated from MORB material (Fig. 7). The melt inclusions in GG16-2 have Al_2O_3 and TiO_2 contents that substantially overlap with melts from secondary pyroxenites at given MgO (Fig. 7c and d). More importantly, the melt inclusions in GG16-2 have low CaO contents compared to peridotitic melts but similar CaO to secondary pyroxenitic melts (Fig. 7b). All of these features are consistent with melts derived from a dominantly pyroxenitic source, as per Sobolev et al. (2005, 2007) or Herzberg (2006, 2011).

The melt composition of the pyroxenite, with or without olivine, is largely controlled by the ratio between reacted clinopyroxene and garnet during melt generation. This ratio is closely related to the mineralogy of the starting material, and the pressure and temperature during melting (Kogiso and Hirschmann, 2001; Kogiso et al., 2003). The starting materials for high-pressure melting of secondary pyroxenite contain about 25% garnet and 75% clinopyroxene, and garnet is consumed earlier than clinopyroxene (Sobolev et al., 2005, 2007). The Al_2O_3 content of the melt will thus decrease while its CaO content increases dramatically if garnet is absent (Kogiso and Hirschmann, 2001), producing melts dissimilar to the high-Si sample of this study. Thus, garnet must have been present in the pyroxenite sources to produce the high-Si basalt of this study.

5.3.2. A carbonated peridotitic/garnet pyroxenitic source for the low-Si basalts

Olivines in the low-Si sample CZ have lower Ni but higher Mn at a given Fo value as compared to those of the high-Si sample GG16-2, much like La Palma picrobasalts (Gurenko et al., 2009; Fig. 6a and b), suggesting a greater percentage of olivine in its source. Magmatic olivines in CZ have Ca contents similar to those in GG16-2 and extend to higher values (Fig. 6c). Their corresponding melt inclusions have higher CaO contents than are observed in GG16-2 inclusions at given MgO (Fig. 7b). These different Fo–Ca correlations indicate that magma evolution has different effects on the Ca partitioning in olivine in the high- and low-Si lavas.

The melt inclusions in sample CZ have lower SiO_2 and higher CaO contents than are commonly observed in melts of peridotite or secondary pyroxenite (Fig. 8a), but are similar to melts generated from carbonated eclogite (SLEC1 + 5 wt% CO_2; Dasgupta et al., 2006) and carbonated peridotite (KLB-1 + 1.0 wt% CO_2; Dasgupta et al., 2007). However, the CZ host lava cannot be derived exclusively from a carbonated peridotitic source, as suggested by Zeng et al. (2010), because its CaO contents are too low relative to melts formed from carbonated peridotite (KLB-1 + 1.0 wt% CO_2; Dasgupta et al., 2007; Fig. 7b). In addition, CZ has higher TiO_2 contents than are observed in peridotitic melts, with or without carbonate, suggesting the presence of other enriched components in its source (Fig. 7d). Clinopyroxene in the mantle will significantly buf-

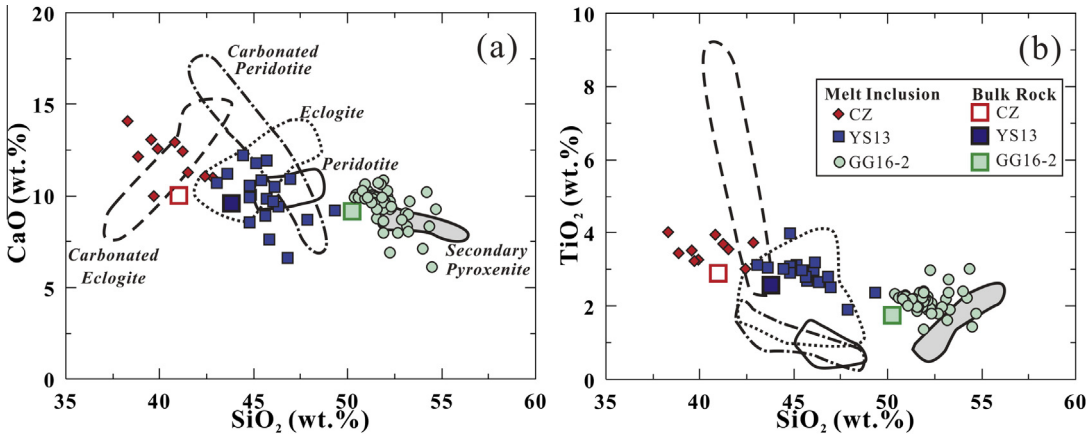

Fig. 8. CaO (a) and TiO_2 (b) versus SiO_2 plots of olivine hosted melt inclusions for basalts from western Shandong and the Bohai Bay Basin, compared with high-pressure experimental melts of carbonate-bearing and -free materials. Pressure, starting materials and data source: Secondary Pyroxenite: 3.5 GPa, Px-1 (Sobolev et al., 2007); Carbonated Eclogite: 3.0 GPa, SLEC1 + 5.0 wt% CO_2 (Dasgupta et al., 2006); Peridotite: 2.5–3.0 GPa, HK-66 and KLB-1 (Hirose and Kushiro, 1993); Carbonated Peridotite: 3.0 GPa, KLB-1 + 1.0% CO_2 (Dasgupta et al., 2007); Eclogite: 2.0–5.0 GPa, KLB-1 + MORB (Kogiso et al., 1998), MIX1G (Hirschmann et al., 2003), BECL (Kogiso and Hirschmann, 2006).

fer CaO. Silicate-rich melts from carbonated eclogite (SLEC1 + 5 wt% CO_2; Dasgupta et al., 2006) at low melt extents (<12%) have low CaO (<8.4%). Therefore, a peridotite mantle source hybridized with garnet pyroxenite in the presence of carbonate may be a suitable source for the low-Si lava studied here based on its SiO_2 and CaO contents. Melts of such a source will also crystallize olivines with the Ni–Mn signatures that are observed in CZ (Fig. 6a and b).

The presence of carbonate in the source for sample CZ is further supported by the observed negative Zr, Hf, and Ti anomalies seen on a primitive-mantle normalized spidergram (Fig. 4a; Zeng et al., 2010), because $D_i^{bulk/melts}$ for Zr, Hf, and Ti are higher than those of the middle REEs (Nd, Sm, Eu and Gd) in a carbonated mantle source (Dasgupta et al., 2009). In addition, dissolved CO_2 in the low-Si lava may trigger crystallization of low-Ca, high Fo olivines. As CO_3^{2-} ligands complex preferentially with Ca^{2+} cations (Brooker et al., 2001), the stability of Ca in carbonated silicate melts increases. Calculations of $D_{Ca}^{olivine/melts}$ based on the carbonated peridotite melting experiment result of Dasgupta et al. (2007) reveal the residual olivine have higher $D_{Ca}^{olivine/melts}$ under the condition of lower CO_2 content (1%) than that under higher CO_2 content (2.5%) at the same pressure and temperature. CO_2 dissolution triggering crystallization of low-Ca olivine can also explain the precipitation of low-Ca olivine from volatile-rich melts, such as kimberlites (Kamenetsky et al., 2008, 2013) and subduction-related basalts (Kamenetsky et al., 1997, 2006). The inverse correlation between Ca contents and Fo values for olivines from CZ may reflect CO_2 degassing or CO_3^{2-} dilution process during magmatic evolution (Fig. 6c). As the parental magma to CZ became Ca-rich and CO_3^{2-}-poor during differentiation, its olivines begin to take in more Ca. Abundant fluid inclusions in CZ olivines (Fig. 2a and b) also suggest that this parental magma was fluid-rich.

5.4. Contributions from the subducted Pacific plate to the genesis of intracontinental basalts in the eastern NCC

5.4.1. Controls on the chemistries of intracontinental basalts in the eastern NCC

As discussed above, the NCC high-Si basalts are consistent with a derivation from a garnet pyroxenitic mantle source while the low-Si basalts are consistent with a carbonated mantle source.

The garnet pyroxenitic mantle source for the high-Si basalts is not olivine-free, similar to that of Jurassic mafic alkaline basaltic magmatism in the Baltic Shield in Scania, southern Sweden (Tappe et al., 2016). Olivines in the high-Si sample GG16-2 have Ni contents of ~2100–2650 ppm at Fo of ~84 (Fig. 6a), significantly lower than those crystallized from an olivine-free mantle source (up to 3200 ppm at Fo of ~84 in the Koolau case; Sobolev et al., 2005, 2007). The high- to moderate-Si basalts examined in this study were erupted between 23 and 20 Ma (He et al., 2011; Xu et al., 2012b; Zeng et al., 2011), and are not distinguishable in terms of their temporal and spatial distribution. However, the low-Si lavas were erupted much later, including some near present-day occurrences in Penglai and Qixia in Jiaodong Peninsula (8.7–0.3 Ma), and in Dashan of Wudi in western Shandong (<1 Ma; Fig. 1; Luo et al., 2009; Zeng et al., 2010; Sakuyama et al., 2013). Thus, contributions from garnet pyroxenitic and carbonated mantle sources appear to reflect different temporal stages of basalt generation in the eastern NCC.

The melting conditions of the possible source materials for basalts of this study, i.e., peridotite, garnet pyroxenite and carbonated ecologite, have been experimentally examined. The solidus of a carbonated mantle source, either peridotitic, pyroxenitic, or ecologitic, will be crossed under lower P-T conditions than a corresponding carbonate-poor mantle source (e.g., Dasgupta et al., 2004, 2007, 2013). The solidi of carbonated eclogite (~340 km; Dasgupta et al., 2004), carbonated peridotite (~300 km;

Dasgupta et al., 2007), Si-deficient garnet pyroxenite (~70 km; Kogiso et al., 2003), and dry peridotite (~60 km; Hirschmann, 2000) are successively crossed during adiabatic upwelling of the mantle, assuming a 1350 °C mantle potential temperature (e.g., McKenzie et al., 2005).

The chemistry of asthenospheric mantle-derived primitive basaltic lavas depend on not only source composition, but also lithospheric thickness and mantle temperature. Mantle temperature and lithospheric thickness constrain the initial and final melting depths of a melting column in the asthenosphere, assuming a lithospheric lid on melting (e.g., Niu and Batiza, 1991). Higher mantle temperatures correspond to greater initial melting depths, and the shallowest melting depths under a thick lithosphere would be greater than that under a thin lithosphere (e.g., Niu and Batiza, 1991; Fram and Lesher, 1993; Niu et al., 2011).

5.4.2. Hf-Nd isotopes reveal different enriched materials for the high- and low-Si basalts

Higher Ba/Th and lower FeO^T for the high-Si basalts but lower Ba/Th and higher FeO^T for the low-Si basalts (Fig. 4d) suggest that marine sediments and oceanic crust may be the sources of the enriched components of these basalts, respectively (e.g., Kuritani et al., 2011; Sakuyama et al., 2013). To calculate the Hf–Nd isotopic signatures of oceanic crust and marine sediments formed at different times in the Earth's history, we assumed a linear relationship between their isotopic ratios at present and 4.55 Ga, as per Chauvel et al. (2008). Then they were modelled to evolve through time using the present-day average Nd–Hf isotopic compositions, Sm/Nd and Lu/Hf elemental ratios of Global Subducted Sediment and N-MORB (Plank and Langmuir, 1998; Su and Langmuir, 2003; Chauvel et al., 2008), respectively. Modeling results for the Hf and Nd isotopes suggest that the source of the high-Si basalts in western Shandong and the Bohai Bay Basin contains an ancient (~1.0 Ga) recycled component with a strong marine sedimentary signature (Li et al., 2014; Fig. 5b and c), consistent with their high Ba/Th (Fig. 4d). Sr–Nd isotopic correlations indicate that the high-Si basalts may also reflect contributions from an EM1-like mantle source (Fig. 5a), which would have a >1.0 Ga integrated residence time in order to match its isotopic signature (Rehkämper and Hofmann, 1997; Murphy et al., 2003). These inferences argue for the idea that the garnet pyroxenitic sources of the high-Si basalts contain recycled materials associated with ancient subduction as opposed to Pacific plate subduction (Kuritani et al., 2011), as the Pacific plate is suggested to have started subduction beneath the eastern NCC from Jurassic or Cretaceous time (Maruyama et al., 1997; Müller et al., 2008). By contrast, the studied low-Si basalts carry the Hf–Nd isotopic fingerprint of Pacific ocean crust, and their enriched component is younger than that of the high-Si basalts (Fig. 5b and c). Our estimated age of ~500 Ma is close to the age of the oldest subducted Pacific plate crust (>300 Ma, based on plate reconstructions of Müller et al., 2008). A Ba, Sr and Pb-rich garnet pyroxenite mantle source with low ε_{Hf} and ε_{Nd} values for the high-Si basalts, but a Ba, Sr and Pb poor carbonated mantle source for the low-Si basalts suggest that their enriched components are not derived from a single subduction episode, consistent with the decoupling of the likely ages of their enriched components (Fig. 5b and c).

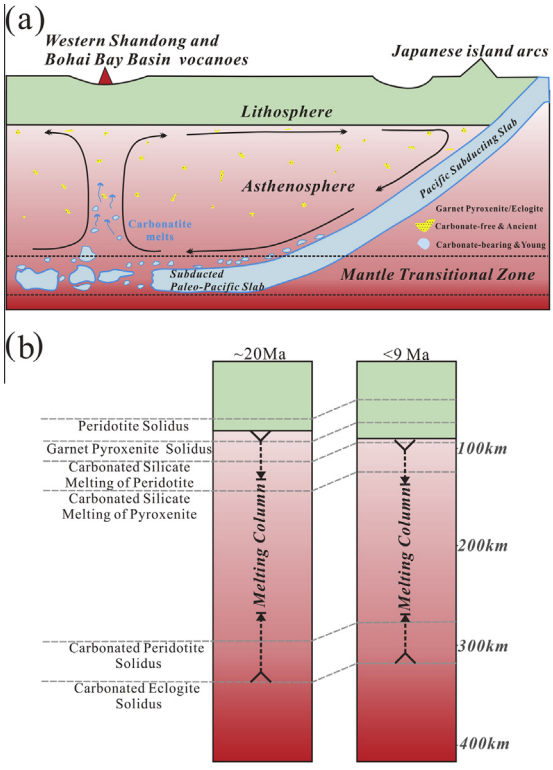

Fig. 9. Cartoon illustrating mantle heterogeneity and the generation of intraplate basalts in the eastern NCC. (a) Asthenospheric mantle beneath the eastern NCC, including dispersed zones of garnet pyroxenite with EM1 isotopic signature, is metasomatized by carbonatite melts/fluids from carbonated eclogite of the subducted Pacific slab in the mantle transition Zone; (b) Thickening of the lithosphere and associated changes in the lengths of mantle melting columns explains the temporal chemical evolution of the basaltic lavas. At ~20 Ma, when the lithosphere was relatively thin, high degree melting of the garnet pyroxenite in the shallow mantle generated high-Si lavas with EM1 isotopic signature. Mixing of melts from garnet pyroxenite and a deep carbonated source generated moderate-Si lavas. After 9 Ma, when the lithosphere is thick and the potential temperature of the mantle is low, garnet pyroxenite cannot melt. Low degree melting of the carbonated deep mantle source (peridotitic and garnet pyroxenitic) produced low-Si lavas with isotopic signature akin to the Pacific Ocean crust.

5.4.3. Contributions from the subducted Pacific slab

To account for the temporal and spatial variation of basalts with differing SiO_2, trace element and isotopic characteristics in the eastern NCC, we propose a model for dynamic melting of a mantle source affected by oceanic subduction in association with lithospheric evolution. Fig. 9a outlines the likely circumstances that have developed in the deep mantle beneath the NCC, with pre-existing garnet pyroxenitic domains derived from ancient subduction, and carbonated eclogitic materials derived from subducted Pacific slab contributing to convectively upwelling NCC

mantle. "Blobs" of subducted material dispersed in a depleted peridotite matrix is said to be common in the upper asthenospheric mantle (see the review by Fitton, 2007). We therefore posit that there are present in the NCC asthenospheric mantle dispersed domains of garnet-bearing pyroxenites resulting from reactions between recycled ancient (>1.0 Ga) materials (rich in marine sediments) and peridotite (Fig. 9a). Subduction of the Pacific plate further hybridized the mantle, with the stagnation of subducted oceanic crust in the mantle transition zone beneath the eastern NCC (Fig. 9a). As some carbonate can be retained to greater depths in subducted oceanic crust (Sleep and Zahnle, 2001), the oceanic crust would be transformed into carbonated eclogites. Because carbonated eclogite is below its solidus temperature when initially recycled into the mantle, carbonates can be transported to the mantle transition zone without melting, as suggested by Dasgupta and Hirschmann (2010) and Sakuyama et al. (2013). "Plums" of the recycled oceanic crust, or the leading edge of the subducted oceanic section (Sakuyama et al., 2013) would slowly warm and come into thermal equilibrium with the deep mantle.

Contemporaneously with the extension of the eastern Asian continental margin, the eastern NCC experienced strong rifting and the Bohai Bay Basin began to subside during the Eocene–Oligocene, indicating significant upwelling of the asthenospheric mantle beneath the BBB (Hu et al., 2001; Li et al., 2014). Small carbonated eclogite "plums" in the upwelling mantle would cross their solidi first along a mantle adiabat at about 340 km. Carbonatite melts generated from carbonated eclogite at depths of ~340 km (Dasgupta et al., 2004) will be enriched in FeO^T and incompatible trace elements (Dasgupta et al., 2006), and will carry them the isotopic signatures of those eclogites. Carbonatite melts would migrate freely upward to shallower depths and would lead to shallower mantle sources becoming metasomatized (Fig. 9a). Migrating carbonatite liquids interacting with garnet pyroxenite and peridotite at shallower depths (130–110 km; Dasgupta et al., 2007) will result in carbonated silicate melts that are enriched of FeO^T and incompatible trace elements.

Based on sedimentological data, extension in the eastern NCC, (i.e., rifting of the BBB) terminated around 23 Ma (Hu et al., 2001; Qi and Yang, 2010). Analysis of the region's thermal history, based vitrinite reflectance and apatite fission track data, indicate that the eastern NCC experienced a period of much higher paleo–heat flow (70–90 mW/m^2) at ~23 Ma with subsequent thermal decay to the present of ~63 mW/m^2 (Hu et al., 2001). As the heat flow value is negatively correlated with the lithospheric thickness (He, 2015), the paleo–heat flow data indicate the extension of the eastern NCC led to a thinner lithosphere at ~23 Ma than at present (80–100 km; Chen, 2010), and subsequent thermal decay likely related to the vertical lithospheric accretion (Xu, 2001; Xu et al., 2009). In the case of a thin lithosphere (<70 km) at ~23–20 Ma (Fig. 9b), high degree melting of garnet pyroxenites from a shallow mantle source would yield the high-Si lavas like GG16-2 (Fig. 3), with low trace element concentrations (Fig. 4a) and low ε_{Hf} and ε_{Nd}, showing strong Hf-Nd isotope affinities with subducted sediments (Fig. 5b and c). Mixing between high degree melts of garnet pyroxenite and low degree melts of the deeper, carbonated peridotite/garnet pyroxenite could produce the moderate-Si lavas, with intermediate trace element concentrations and intermediate Hf–Nd isotopic signatures. A thickened lithosphere resulting from thermal decay at <9 Ma (Xu, 2001; Xu et al., 2009) discouraged melting of secondary garnet pyroxenite as its adiabat and its solidus no longer cross (Fig. 9b). In this circumstance, only the carbonated deep mantle sources (peridotitic and garnet pyroxenitic) will melt, resulting in the formation of low-Si lavas with higher trace element concentrations (Fig. 4a) and higher ε_{Hf}~ ε_{Nd}, similar isotopically to Pacific oceanic crust (Fig. 5b and c).

6. CONCLUSIONS

Three groups of Cenozoic basalts have been identified in the western Shandong and Bohai Bay Basin, of the eastern NCC: (1) high-Si and (2) moderate-Si basalts (tholeiites, alkali basalts and basanites) erupted between 23 and 20 Ma, and (3) low-Si basalts (nephelinites) erupted since 9 Ma. The high-Si basalts have lower alkalies, CaO and FeO^T contents, lower trace element concentrations, lower La/Yb, Sm/Yb and Ce/Pb but higher Ba/Th ratios than the low-Si basalts. The high-Si samples have less radiogenic Hf–Nd isotopes showing signature of the Indian Ocean mantle domain, while the low-Si samples have more radiogenic Hf–Nd isotopes akin to the Pacific Ocean mantle domain. The olivines in the high-Si basalts have higher Ni and lower Mn and Ca at a given Fo value than those crystallizing from peridotite melts, with their corresponding melt inclusions have lower CaO contents than peridotite melts, suggesting a garnet pyroxenitic source. The magmatic olivines from low-Si basalts have lower Ni but higher Mn at a given Fo value than that of the high-Si basalts, suggesting more olivine in its source than that of the high-Si basalts. The olivine-hosted melt inclusions of the low-Si basalts have the major element signatures different from those of normal peridotitic or garnet pyroxenitic mantle sources, pointing to melts from carbonated mantle sources. The chemical evolution of Cenozoic basalts from the western Shandong and Bohai Bay Basin suggests their petrogenesis is attributable to the differential melting of hybridized mantle sources beneath the eastern NCC, induced by the subduction of Pacific plate in association with lithospheric evolution. Asthenospheric mantle beneath the eastern NCC, intermixed with garnet pyroxenites with an EM1 isotopic signature, was metasomatized by carbonatite from carbonated eclogites derived from deeply subducted Pacific slab. When the lithospheric mantle was relatively thin between 23 and 20 Ma, high degree melting of garnet pyroxenites at shallow mantle depths produced high-Si lavas. By 9 Ma a thickening lithosphere permitted only low degree melting of carbonated deep mantle sources, producing low-Si lavas. Moderate-Si lavas erupted at ~20 Ma are consistent with mixtures of high- and low-Si lavas.

ACKNOWLEDGMENTS

We appreciate Jinlong Ma and Lei Wu for analytical assistance. We gratefully acknowledge Marc Norman, Michael Rowe and an anonymous reviewer for their constructive and thoughtful comments that helped improve the manuscript. Editorial handling by Marc Norman is greatly appreciated. The research was supported by the National Natural Science Foundation of China (NSFC Projects 41273042, 91214202, 41472210). This is contribution No. IS–2172 to GIG-CAS.

APPENDIX A. SUPPLEMENTARY DATA

Supplementary data associated with this article can be found, in the online version, at http://dx.doi.org/10.1016/j.gca.2015.12.032.

REFERENCES

Allen M. B., Macdonald D. I. M., Zhao X., Vincent S. J. and Brouet-Menzies C. (1997) Early Cenozoic two-phase extension and late Cenozoic thermal subsidence and inversion of the Bohai Basin, North China. *Mar. Petrol. Geol.* **14**, 951–972.

Balta J. B., Asimow P. D. and Mosenfelder J. L. (2011) Manganese partitioning during hydrous melting of peridotite. *Geochim. Cosmochim. Acta* **75**, 5819–5833.

Beattie P., Ford C. and Russell D. (1991) Partition coefficients for olivine^melt and orthopyroxene^melt systems. *Contrib. Miner. Petrol.* **109**, 212–224.

Blichert-Toft J. and Albarède F. (1997) The Lu–Hf isotope geochemistry of chondrites and the evolution of the mantle-crust system. *Earth Planet. Sci. Lett.* **148**(1–2), 243–258.

Brooker R. A., Kohn S. C., Holloway J. R. and McMillan P. F. (2001) Structural controls on the solubility of CO_2 in silicate melts Part II: IR characteristics of carbonate groups in silicate glasses. *Chem. Geol.* **174**, 241–254.

Carmichael I. S. E. and Ghiorso M. S. (1986) Oxidation–reduction relations in basic magma: a case for homogeneous equilibria. *Earth Planet. Sci. Lett.* **78**, 200–210.

Chauvel C., Lewin E., Carpentier M., Arndt N. T. and Marini J. C. (2008) Role of recycled oceanic basalt and sediment in generating the Hf–Nd mantle array. *Nat. Geosci.* **1**, 64–67.

Chen L. H., Zeng G., Jiang S. Y., Hofmann A. W., Xu X. S. and Pan M. B. (2009) Sources of Anfengshan basalts: Subducted lower crust in the Sulu UHP belt, China. *Earth Planet. Sci. Lett.* **286**, 426–435.

Chen L. (2010) Concordant structural variations from the surface to the base of the upper mantle in the North China Craton and its tectonic implications. *Lithos* **120**, 96–115.

Chu Z. Y., Wu F. Y., Walker R. J., Rudnick R. L., Pitcher L., Puchtel I. S., Yang Y. H. and Wilde S. A. (2009) Temporal evolution of the lithospheric mantle beneath the eastern North China Craton. *J. Petrol.* **50**, 507–529.

Danyushevsky L. V., Della-Pasqua F. N. and Sokolov S. (2000) Re-equilibration of melt inclusions trapped by magnesian olivine phenocrysts from subduction-related magmas: petrological implications. *Contrib. Miner. Petrol.* **138**, 68–83.

Danyushevsky L. V. and Plechov P. (2011) Petrolog 3: integrated software for modeling crystallization processes. *Geochem. Geophys. Geosyst.* **12**, Q07021. http://dx.doi.org/10.1029/2011GC003516.

Dasgupta R. and Hirschmann M. M. (2010) The deep carbon cycle and melting in Earth's interior. *Earth Planet. Sci. Lett.* **298**, 1–13.

Dasgupta R., Hirschmann M. M. and Smith N. D. (2007) Partial melting experiments of peridotite CO_2 at 3 GPa and genesis of alkalic ocean island basalts. *J. Petrol.* **48**, 2093–2124.

Dasgupta R., Hirschmann M. M., McDonough W. F., Spiegelman M. and Withers A. C. (2009) Trace element partitioning between garnet lherzolite and carbonatite at 6.6 and 8.6 GPa with applications to the geochemistry of the mantle and of mantle-derived melts. *Chem. Geol.* **262**, 57–77.

Dasgupta R., Hirschmann M. M. and Stalker K. (2006) Immiscible transition from carbonaterich to silicate-rich melts in the 3 GPa melting interval of eclogite plus CO_2 and genesis of silica-undersaturated ocean island lavas. *J. Petrol.* **47**, 647–671.

Dasgupta R., Hirschmann M. M. and Withers A. C. (2004) Deep global cycling of carbon constrained by the solidus of anhydrous, carbonated eclogite under upper mantle conditions. *Earth Planet. Sci. Lett.* **227**, 73–85.

Dasgupta R., Mallik A., Tsuno K., Withers A. C., Hirth G. and Hirschmann M. M. (2013) Carbon-dioxide-rich silicate melt in the Earth's upper mantle. *Nature* **493**, 211–216.

Fan Q. C. and Hooper P. R. (1991) The Cenozoic basaltic rocks of eastern China: petrology and chemical composition. *J. Petrol.* **32**, 765–810.

Fitton J. G. (2007) The OIB paradox. *The Geological Society of America Special Paper* **430**, 387–412.

Ford C. E., Russell D. G., Craven J. A. and Fisk M. R. (1983) Olivine–liquid equilibria: temperature, pressure, and composition dependence of the crystal/liquid cation partition coefficient for Mg, Fe^{2+}, Ca and Mn. *J. Petrol.* **24**, 256–266.

Fram M. S. and Lesher C. F. (1993) Geochemical constraints on mantle melting during creation of the North Atlantic basin. *Nature* **363**, 712–715.

Fukao Y., Obayashi M., Inoue H. and Nenbai M. (1992) Subducting slab stagnant in the mantle transition zone. *J. Geophys. Res.* **97**, 4809–4822.

Green D. H. and Ringwood A. E. (1967) The genesis of basaltic magmas. *Contrib. Miner. Petrol.* **15**, 103–190.

Gurenko A. A., Sobolev A. V., Hoernle K. A., Hauff F. and Schmincke H. U. (2009) Enriched, HIMU–type peridotite and depleted recycled pyroxenite in the Canary plume: a mixed-up mantle. *Earth Planet. Sci. Lett.* **277**, 514–524.

Hart S. R. and Davis K. E. (1978) Nickel partitioning between olivine and silicate melt. *Earth Planet. Sci. Lett.* **40**, 203–219.

Hauri E. H. (1996) Major element variability in the Hawaiian mantle plume. *Nature* **382**, 415–419.

He H. Y., Deng C. L., Pan Y. X., Deng T., Luo Z. H., Sun J. M. and Zhu R. X. (2011) New $^{40}Ar/^{39}Ar$ dating results from the Shanwang Basin, eastern China: constraints on the age of the Shanwang Formation and associated biota. *Phys. Earth Planet. Inter.* **187**, 66–75.

He L. J. (2015) Thermal regime of the North China Craton: implications for craton destruction. *Earth Sci. Rev.* **140**, 14–26.

Herzberg C. (2006) Petrology and thermal structure of the Hawaiian plume from Mauna Kea volcano. *Nature* **444**, 605–609.

Herzberg C. (2011) Identification of source lithology in the Hawaiian and Canary Islands: implications for origins. *J. Petrol.* **52**, 113–146.

Herzberg C. and Asimow P. D. (2008) Petrology of some oceanic island basalts: PRIMELT2.XLS software for primary magma calculation. *Geochem. Geophys. Geosyst.* **8**, Q09001. http://dx.doi.org/10.1029/2008GC002057.

Hirose K. and Kushiro I. (1993) Partial melting of dry peridotites at high pressures: determination of compositions of melts segregated from peridotite using aggregates of diamond. *Earth Planet. Sci. Lett.* **114**, 477–489.

Hirschmann M. M. (2000) The mantle solidus: experimental constraints and the effect of peridotite composition. *Geochem. Geophys. Geosyst.* **1**. http://dx.doi.org/10.1029/2000GC000070, Paper number 2000GC000070.

Hirschmann M. M., Kogiso T., Baker M. B. and Stolper E. M. (2003) Alkalic magmas generated by partial melting of garnet pyroxenite. *Geology* **31**, 481–484.

Hofmann A. W. (1997) Mantle geochemistry: the message from oceanic volcanism. *Nature* **385**, 219–229.

Hong L. B., Zhang Y. H., Qian S. P., Liu J. Q., Ren Z. Y. and Xu Y. G. (2013) Constraints from melt inclusions and their host olivines on the petrogenesis of Oligocene-Early Miocene Xindian basalts, Chifeng area, North China Craton. *Contrib. Miner. Petrol.* **165**(2), 305–326.

Hu S. B., O'Sullivan P. B., Raza A. and Kohn B. P. (2001) Thermal history and tectonic subsidence of the Bohai Basin, northern China: a Cenozoic rifted and local pull-apart basin. *Phys. Earth Planet. Inter.* **126**, 221–235.

Huang X. L., Niu Y. L., Xu Y. G., Ma J. L., Qiu H. N. and Zhong J. W. (2013) Geochronology and geochemistry of Cenozoic basalts from eastern Guangdong, SE China: constraints on the lithosphere evolution beneath the northern margin of the South China Sea. *Contrib. Miner. Petrol.* **165**, 437–455.

Jacobsen S. B. and Wasserburg G. J. (1980) Sm-Nd isotopic evolution of chondrites. *Earth Planet. Sci. Lett.* **50**(1), 139–155.

Kamenetsky V. S., Crawford A. J., Eggins S. and Mühe R. (1997) Phenocryst and melt inclusion chemistry of near-axis seamounts, Valu Fa Ridge, Lau Basin: insight into mantle wedge melting and the addition of subduction components. *Earth Planet. Sci. Lett.* **151**, 205–223.

Kamenetsky V. S., Elurg M., Arculus R. and Thomas R. (2006) Magmatic origin of low-Ca olivine in subduction related magmas: co-existence of contrasting magmas. *Chem. Geol.* **233**, 346–357.

Kamenetsky V. S., Grütter H., Kamenetsky M. B. and Gömann K. (2013) Parental carbonatitic melt of the Koala kimberlite (Canada): constraints from melt inclusions in olivine and Cr-spinel, and groundmass carbonate. *Chem. Geol.* **353**, 96–111.

Kamenetsky V. S., Kamenetsky M. B., Sobolev A. V., Golovin A. V., Demouchy S., Faure K., Sharygin V. V. and Kuzmin D. V. (2008) Olivine in the Udachnaya-East kimberlite (Yakutia, Russia): types, compositions and origins. *J. Petrol.* **49**, 823–839.

Li X. H., Qi C. S., Liu Y., Liang X. R., Tu X. L., Xie L. W. and Yang Y. H. (2005) Petrogenesis of the Neoproterozoic bimodal volcanic rocks along the western margin of the Yangtze Block: new constraints from Hf isotopes and Fe/Mn ratios. *Chin. Sci. Bull.* **50**, 2481–2486.

Liu D. Y., Nutman A. P., Compston W., Wu J. S. and Shen Q. H. (1992) Remnants of ⩾3800 Ma crust in the Chinese part of the Sino-Korean Craton. *Geology* **20**, 339–342.

Liu J. G., Rudnick R., Walker R. J., Xu W. L., Gao S. and Wu F. Y. (2015) Big insights from tiny peridotites: evidence for persistence of Precambrian lithosphere beneath the eastern North China Craton. *Tectonophysics* **650**, 104–112.

Kinzler R. J., Grove T. L. and Recca S. I. (1990) An experimental study on the effect of temperature and melt composition on the partitioning of nickel between olivine and silicate melt. *Geochim. Cosmochim. Acta* **54**, 1255–1265.

Kogiso T., Hirose K. and Takahashi E. (1998) Melting experiments on homogeneous mixtures of peridotite and basalt: application to the genesis of ocean island basalts. *Earth Planet. Sci. Lett.* **162**, 45–61.

Kogiso T. and Hirschmann M. M. (2001) Experimental study of clinopyroxenite partial melting and the origin of ultra-calcic melt inclusions. *Contrib. Miner. Petrol.* **142**, 347–360.

Kogiso T. and Hirschmann M. M. (2006) Partial melting experiments of bimineralic eclogite and the role of recycled mafic oceanic crust in the genesis of ocean island basalts. *Earth Planet. Sci. Lett.* **249**, 188–199.

Kogiso T., Hirschmann M. M. and Frost D. J. (2003) High-pressure partial melting of garnet pyroxenite: possible mafic lithologies in the source of ocean island basalts. *Earth Planet. Sci. Lett.* **216**, 603–617.

Kuang Y. S., Wei X., Hong L. B., Ma J. L., Pang C. J., Zhong Y. T., Zhao J. X. and Xu Y. G. (2012) Petrogenetic evaluation of the Laohutai basalts from North China Craton: melting of a two-component source during lithospheric thinning in the late Cretaceous–early Cenozoic. *Lithos* **154**, 68–82.

Kuritani T., Ohtani E. and Kimura J. I. (2011) Intensive hydration of the mantle transition zone beneath China caused by slab stagnation. *Nat. Geosci.* **4**, 713–716.

Li H. Y., Huang X. L. and Guo H. (2014) Geochemistry of Cenozoic basalts from the Bohai Bay Basin: implications for a heterogeneous mantle source and lithospheric evolution beneath the eastern North China Craton. *Lithos* **196–197**, 54–66.

Liu Y. S., Gao S., Kelemen P. B. and Xu W. L. (2008) Recycled crust controls contrasting source compositions of Mesozoic and Cenozoic basalts in the North China Craton. *Geochim. Cosmochim. Acta* **72**, 2349–2376.

Luo D., Chen L. H. and Zeng G. (2009) Genesis of intra–continental strongly alkaline volcanic rocks: a case study of Dashan nephelinites in Wudi, Shandong Province, North China. *Acta Petrologica Sinica* **25**, 311–319.

Maruyama S., Isozaki Y., Kimura G. and Terabayashi M. (1997) Paleogeographic maps of the Japanese Islands: plate tectonic synthesis from 750 Ma to the present. *Island Arc* **6**, 121–142.

McDonough W. F. and Sun S. S. (1995) The composition of the Earth. *Chem. Geol.* **120**, 223–253.

McKenzie D., Jackson J. and Priestley K. (2005) Thermal structure of oceanic and continental lithosphere. *Earth Planet. Sci. Lett.* **233**, 337–349.

McKenzie D. P. and O'Nions R. K. (1991) Partial melt distributions from inversion of rare earth element concentrations. *J. Petrol.* **32**, 1021–1091.

Murphy D. T., Kamber B. S. and Collerson K. D. (2003) A refined solution to the first terrestrial Pb-isotope paradox. *J. Petrol.* **44**, 39–53.

Müller R. D., Sdrolias M., Gaina C., Steinberger B. and Heine C. (2008) Long-term sea-level fluctuations driven by ocean basin dynamics. *Science* **319**, 1357–1362.

Niu Y. L. and Batiza R. (1991) An empirical method for calculating melt compositions produced beneath mid-ocean ridges: application for axis and off-axis (seamounts) melting. *J. Geophys. Res.* **96**, 21753–21777.

Niu Y. L. and O'Hara M. J. (2003) Origin of ocean island basalts: a new perspective from petrology, geochemistry, and mineral physics considerations. *J. Geophys. Res.* **108**(B4), 2209.

Niu Y. L., Wilson M., Humphreys E. R. and O'Hara M. J. (2011) The origin of intra-plate Ocean Island Basalts (OIB): the lid effect and its geodynamic implications. *J. Petrol.* **52**, 1443–1468.

O'Reilly S. Y. and Zhang M. (1995) Geochemical characteristics of lava-field basalts from eastern Australia and inferred sources: connections with the subcontinental lithospheric mantle? *Contrib. Miner. Petrol.* **121**, 148–170.

Pertermann M. and Hirschmann M. M. (2003) Anhydrous partial melting experiments on MORB-like eclogite: phase relations, phase compositions and mineral-melt partitioning of major elements at 2–3GPa. *J. Petrol.* **44**, 2173–2201.

Pearce J. A., Kempton P. D., Nowell G. M. and Noble S. R. (1999) Hf-Nd element and isotope perspective on the nature and

provenance of mantle and subduction components in Western Pacific arc-basin systems. *J. Petrol.* **40**(11), 1579–1611.

Plank T. and Langmuir C. H. (1998) The chemical composition of subducting sediment and its consequences for the crust and mantle. *Chem. Geol.* **145**, 325–394.

Putirka K., Ryerson F. J., Perfitt M. and Ridley W. I. (2011) Mineralogy and composition of the oceanic mantle. *J. Petrol.* **52**, 279–313.

Qi J. F. and Yang Q. (2010) Cenozoic structural deformation and dynamic processes of the Bohai Bay basin province, China. *Mar. Pet. Geol.* **27**, 757–771.

Qin X. F. (2008) *Geochronology and geochemistry of the Tertiary basalts from the Midanjiang-Mishan regions: mantle source characteristics and its spatial–temporal evolution* Ph.D. dissertation. Graduate School of Chinese Academy of Sciences, Beijing, 125.

Ren Z. Y., Hanyu T., Miyazaki T., Chang Q., Kawabata H., Takahashi T., Hirahara Y., Nichols A. R. L. and Tatsumi Y. (2009) Geochemical differences of the Hawaiian shield lavas: implications for melting process in the heterogeneous Hawaiian plume. *J. Petrol.* **50**, 1553–1573.

Ren Z. Y., Ingle S., Takahashi E., Hirano N. and Hirata T. (2005) The chemical structure of the Hawaiian mantle plume. *Nature* **436**, 837–840.

Ren Z. Y., Shibata T., Yoshikawa M., Johnson K. and Takahashi E. (2006) Isotope compositions of submarine Hana ridge lavas, Haleakala volcano, Hawaii. *J. Petrol.* **45**, 2067–2099.

Rehkämper M. and Hofmann A. W. (1997) Recycled ocean crust and sediment in Indian Ocean MORB. *Earth Planet. Sci. Lett.* **147**, 93–106.

Rudnick R. L. and Gao S. (2003) Composition of the continental crust. In *Treatise on Geochemistry* (ed. R. L. Rudnick). Elsevier, pp. 1–64.

Sakuyama T., Tian W., Kimura J., Fukao Y., Hirahara Y., Takahashi T., Senda R., Chang Q., Miyazaki T., Obayashi M., Kawabata h. and Tatsumi Y. (2013) Melting of dehydrated oceanic crust from the stagnant slab and of the hydrated mantle transition zone: constraints from Cenozoic alkaline basalts in eastern China. *Chem. Geol.* **359**, 32–48.

Schiano P. (2003) Primitive mantle magmas recorded as silicate melt inclusions in igneous minerals. *Earth Sci. Rev.* **63**, 121–144.

Sleep N. H. and Zahnle K. (2001) Carbon dioxide cycling and implications for climate on ancient Earth. *J. Geophys. Res.* **106**, 1373–1399.

Straub S. M., LaGatta A. B., Martin-Del Pozzo A. L. and Langmuir C. H. (2008) Evidence from high-Ni olivines for a hybridized peridotite/pyroxenite source for orogenic andesites from the central Mexican Volcanic Belt. *Geochem. Geophys. Geosyst.* **9**, Q03007. http://dx.doi.org/10.1029/2007GC001583.

Streckeisen A. (1976) To each plutonic rock its proper name. *Earth Sci. Rev.* **12**, 1–33.

Sobolev A. V., Hofmann A. W., Brügmann B., Batanova V. G. and Kuzmin D. V. (2008) A quantitative link between recycling and osmium isotopes. *Science* **321**, 536.

Sobolev A. V., Hofmann A. W., Kuzmin D. V., Yaxley G. M., Arndt N. T., Chung S. L., Danyushevsky L. V., Elliott T., Frey F. A., Garcia M. O., Gurenko A. A., Kamenetsky V. S., Kerr A. C., Krivolutskaya N. A., Matvienkov V. V., Nikogosian I. K., Rocholl A., Sigurdsson I. A., Sushchevskaya N. M. and Teklay M. (2007) The amount of recycled crust in source of mantle-derived melts. *Nature* **316**, 412–417.

Sobolev A. V., Hofmann A. W., Sobolev S. V. and Nikogosian I. K. (2005) An olivine-free mantle source of Hawaiian shield basalts. *Nature* **434**, 590–597.

Stracke A., Hofmann A. W. and Hart S. R. (2005) FOZO, HIMU, and the rest of the mantle zoo. *Geochem. Geophys. Geosyst.* **6**, Q05007. http://dx.doi.org/10.1029/2004GC000824.

Su Y. and Langmuir C. H. (2003) *Global MORB chemistry compilation at the segment scale* PhD thesis. Department of Earth and Environmental Sciences, Columbia University. Available at: http://petdb.ldeo.columbia.edu/documentation/morbcompilation/.

Sun S. S. and McDonough W. F. (1989) Chemical and isotopic systematics of oceanic basalts: implications for mantle composition and processes. In *Magmatism in the Ocean Basins, 42* (eds. A. D. Saunders and M. J. Norry). Geological Society Special Publication, London, pp. 313–345.

Sun W. D., Ding X., Hu Y. H. and Li X. H. (2007) The golden transformation of the Cretaceous plate subduction in the west Pacific. *Earth Planet. Sci. Lett.* **262**, 533–542.

Tang Y. C., Obayashi M., Niu F. L., Grand S. P., Chen Y. J., Kawakatsu H., Tanaka S., Ning J. Y. and Ni J. F. (2014) Changbaishan volcanism in northeast China linked to subduction-induced mantle upwelling. *Nat. Geosci.* **7**, 470–474.

Tappe S., Smart K. A., Stracke A., Romer R. L., Prelević D. and van den Bogaard P. (2016) Melt evolution beneath a rifted craton edge: $^{40}Ar/^{39}Ar$ geochronology and Sr–Nd–Hf–Pb isotope systematics of primitive alkaline basalts and lamprophyres from the SW Baltic Shield. *Geochim. Cosmochim. Acta* **173**, 1–36.

van Keken P. E., Hacker B. R., Syracuse E. M. and Abers G. A. (2011) Subduction factory: 4. Depth-dependent flux of H2O from subducting slabs worldwide. *J. Geophys. Res.* **116**, B01401. http://dx.doi.org/10.1029/2010JB007922.

Wang Z. R. and Gaetani G. A. (2008) Partitioning of Ni between olivine and siliceous eclogite partial melt: experimental constraints on the mantle source of Hawaiian basalts. *Contrib. Miner. Petrol.* **156**, 661–678.

Weis D., Kieffer B., Maerschalk C., Pretorius W. and Barling J. (2005) High-precision Pb-Sr-Nd-Hf isotopic characterization of USGS BHVO-1 and BHVO-2 reference materials. *Geochem. Geophys. Geosyst.* **6**, Q02002. http://dx.doi.org/10.1029/2004GC000852.

White W. M. and Hofmann A. W. (1982) Sr and Nd isotope geochemistry of oceanic basalts and mantle evolution. *Nature* **29**, 821–825.

Willbold M. and Stracke A. (2006) Trace element composition of mantle end-members: implications for recycling of oceanic and upper and lower continental crust. *Geochem. Geophys. Geosyst.* **7**, Q04004. http://dx.doi.org/10.1029/2005GC001005.

Xu Y. G. (2001) Thermo-tectonic destruction of the Archean lithospheric keel beneath eastern China: evidence, timing and mechanism. *Physics and Chemistry of the Earth (A)* **26**, 747–757.

Xu Y. G., Li H. Y., Pang C. J. and He B. (2009) On the time and duration of the destruction of the North China Craton. *Chin. Sci. Bull.* **54**, 3379–3396.

Xu Y. G. (2014) Recycled oceanic crust in the source of 90–40 Ma basalts in North and Northeast China: evidence, provenance and significance. *Geochim. Cosmochim. Acta* **143**, 49–67.

Xu Y. G., Zhang H. H., Qiu H. N., Ge W. C. and Wu F. Y. (2012a) Oceanic crust components in continental basalts from Shuangliao, Northeast China: derived from the mantle transition zone? *Chem. Geol.* **328**, 168–184.

Xu Z., Zhao Z. F. and Zheng Y. F. (2012b) Slab–mantle interaction for thinning of cratonic lithospheric mantle in North China: geochemical evidence from Cenozoic continental basalts in central Shandong. *Lithos* **146**, 202–217.

Yang J. H., Wu F. Y., Wilde S. A., Belousova E. and Griffin W. L. (2008) Mesozoic decratonization of the North China block. *Geology* **36**(6), 467–470.

Zeng G., Chen L. H., Hofmann A. W. and Xu X. S. (2011) Crust recycling in the sources of two parallel volcanic chains in Shandong, North China. *Earth Planet. Sci. Lett.* **302**, 359–368.

Zeng G., Chen L. H., Xu X. S., Jiang S. Y. and Hofmann A. W. (2010) Carbonated mantle sources for Cenozoic intra–plate alkaline basalts in Shandong, North China. *Chem. Geol.* **273**, 35–45.

Zhao D. P. (2004) Global tomographic images of mantle plumes and subducting slabs: insight into deep Earth dynamics. *Phys. Earth Planet. Inter.* **146**, 3–34.

Zhao D. P., Tian Y., Lei J. S., Liu L. C. and Zheng S. H. (2009) Seismic image and origin of the Changbai intraplate volcano in East Asia: role of big mantle wedge above the stagnant Pacific slab. *Phys. Earth Planet. Inter.* **173**, 197–206.

Zhou X. H. and Armstrong R. L. (1982) Cenozoic volcanic rocks of eastern China—secular and geographic trends in chemistry and strontium isotopic composition. *Earth Planet. Sci. Lett.* **59**, 301–329.

Zhu G., Jiang D. Z., Zhang B. L. and Chen Y. (2012a) Destruction of the eastern North China Craton in a backarc setting: evidence from crustal deformation kinematics. *Gondwana Res.* **22**, 86–103.

Zhu R. X., Xu Y. G., Zhu G., Zhang H. F., Xia Q. K. and Zheng T. Y. (2012b) Destruction of the North China Craton. *Science China Earth Sciences* **55**, 1565–1587.

Zindler A. and Hart S. (1986) Chemical geodynamics. *Annu. Rev. Earth Planet. Sci.* **14**, 493–571.

Zou H. B., Zindler A., Xu X. S. and Qi Q. (2000) Major, trace element, and Nd, Sr and Pb isotope studies of Cenozoic basalts in SE China: mantle sources, regional variations, and tectonic significance. *Chem. Geol.* **171**, 33–47.

Associate editor: Marc Norman